

The White Angel: A unique wollastonite-bearing, mass-fractionated refractory inclusion from the Leoville CV3 carbonaceous chondrite

Catherine L. V. CAILLET KOMOROWSKI^{1, 4*}, Ernst K. ZINNER²,
Kevin D. McKEEGAN³, Rick HERVIG⁴, and Peter R. BUSECK^{4, 5}

¹Laboratoire d'Etude de la Matière Extraterrestre CNRS UMS2679,
Muséum National d'Histoire Naturelle, 61 rue Buffon, 75005 Paris, France

²Laboratory for Space Sciences and Physics Department, Washington University, Saint Louis, Missouri 63130, USA

³Department of Earth and Space Sciences, University of California, Los Angeles, California 90095–1567, USA

⁴Arizona State University, School of Earth and Space Exploration, Box 871404, Tempe, Arizona 85287, USA

⁵Arizona State University, Department of Chemistry and Biochemistry, Tempe, Arizona 85287, USA

*Corresponding author. E-mail: ccaillet@mnhn.fr

(Received 13 October 2006; revision accepted 22 April 2007)

Abstract—We report the study of an unusual compact type A refractory inclusion, named the White Angel, from the Leoville CV3 meteorite. The petrologic, mineral chemical, isotopic, and trace-element signatures of this once-molten Ca-Al-rich inclusion (CAI), which contains large, equant wollastonite crystals, indicate a short multistage history that occurred very early, before substantial decay of ²⁶Al. Magnesium in the inclusion is isotopically heavy, with F_{Mg} reaching 18‰/amu, in the range of fractionated and with unidentified nuclear effects (FUN) inclusions. However, the absence of any nuclear anomalies in Ca and Ti and an inferred ²⁶Al/²⁷Al ratio of $(5.5 \pm 0.9) \times 10^{-5}$ indicate that the White Angel belongs to the F inclusions. Silicon and oxygen are also mass fractionated in favor of the heavy isotopes, but to a lesser extent. The O isotopes show a range in ¹⁶O excesses. On an O three-isotope plot, data points lie on a line parallel and to the right of the carbonaceous chondrite anhydrous mineral mixing line, with wollastonite being the most ¹⁶O-rich phase. The chondrite-normalized rare earth and trace-element pattern of the whole inclusion is the complement of an ultrarefractory pattern indicating that precursor phases of the CAI must have condensed in an Al-, heavy rare earth element (HREE)-depleted reservoir. Melting of those precursor phases in an ¹⁶O-rich environment and evaporation led to mass-dependent isotopic fractionation of Mg, Si, and O. Partial isotopic exchange with a reservoir containing unfractionated Mg took place at a later stage but before any measurable decay of ²⁶Al. Some minerals (melilite and perovskite) in the White Angel equilibrated oxygen isotopes with a relatively ¹⁶O-poor reservoir that was also mass-fractionated toward the heavy isotopes, different from that with which the normal or FUN inclusions interacted.

INTRODUCTION

Calcium-aluminum-rich inclusions (CAIs) are thought to be the oldest mineral assemblages formed in the solar nebula. Indeed, their primary mineralogy, first described by Christophe Michel-Levy (1968), mimics assemblages predicted by thermodynamic calculations (Grossman 1972) for condensates from a solar gas cooling from high temperatures, and CAIs have the oldest known Pb-Pb ages of 4567.2 Myr (Amelin et al. 2002). Large isotopic anomalies in FUN CAIs and certain hibonite inclusions indicate that not all presolar material was completely homogenized, however, it appears that most primordial dust was reprocessed in

various ways (e.g., MacPherson et al. 1988). Petrographic features, trace-element abundances, and isotopic mass fractionation demonstrate that multiple melting or reheating episodes were frequently involved in CAI formation (see MacPherson 2003) and the presence of radiogenic ²⁶Mg gives clues regarding the timing of such events. Understanding the formation processes of CAIs represents an important challenge that can provide constraints on large-scale processes in the early solar system. Here we report on a very unusual CAI, a wollastonite-rich inclusion from the Leoville CV3 chondrite named the White Angel (Caillet and Buseck 1992). The White Angel contains a complex record of multiple processes that took place in a variety of early

solar environments. In this paper, we address the genesis of this Al-depleted, supercalcic, type A CAI by using in situ analytical techniques to produce correlated petrographic, chemical, trace-element, and isotopic analyses.

EXPERIMENTAL

Petrography and Mineral Chemistry

The White Angel refractory inclusion (Fig. 1) was observed in two polished thin sections of Leoville. It was studied by optical microscopy, scanning electron microscopy (SEM), electron microprobe analysis (EMPA using wavelength dispersive techniques), and cathodoluminescence. Secondary electron imaging (SEI), backscattered electron imaging (BEI), and wavelength-dispersive X-ray analyses (WDS) were obtained with a JEOL JXA 8600 Superprobe at Arizona State University in Tempe, Arizona, USA, equipped with four crystal spectrometers and a Tracor Northern Series II EDS system. The microprobe was operated at an accelerating voltage of 15 kV and a beam current of 10 nA. The peak and the background counting time for each element was 30 s (occasionally less for Na). The X-ray spatial resolution was $\sim 2 \mu\text{m}$. Standards included synthetic periclase for Mg, synthetic corundum for Al, Johnstown hypersthene for Si, natural wollastonite for Ca, synthetic rutile for Ti, Stillwater chromite for Cr, Broken Hill rhodonite for Mn, Amelia albite for Na, orthoclase for K, synthetic wustite for Fe, synthetic bunsenite for Ni, and V-metal for V. Estimates of the analytical errors were obtained by measuring at least ten points under a stationary beam. Additional measurements were performed at the Max-Planck-Institut für Kernphysik in Heidelberg, Germany, with a computer-controlled, fully automated ARL-SEMQ electron microprobe equipped with wavelength-dispersive spectrometers and operated at 15 kV accelerating voltage. The sample current was set to 15 nA on the brass sample holder to allow checks of the electron beam drift within short intervals. A special analysis program was employed that allows continuous checking of the electron beam position during an analytical run to ascertain that no spatial drift to a neighboring phase had occurred, as well as the readjustment of the beam spot to the desired position in case beam drift had taken place. Long-duration measurements (100 s) were conducted on perovskite to obtain good counting statistics for the minor elements. Pure, synthetic, stoichiometric perovskite standards were measured under the same conditions in 30-minute intervals between analyses of perovskite in the CAI to insure the accuracy of the measured elemental concentrations. Analyses were corrected for dead time, background, beam drift, and matrix effects by applying the procedures of Bence and Albee (1968) and Albee and Ray (1971) for oxides and silicates. Matrix effects were also corrected using Tracor-Northern ZAF matrix correction procedures at ASU.

Isotopic Analysis

Isotopic measurements were made with a Cameca IMS 3f ion microprobe at Washington University. Analyses for Mg were performed following the procedures of McKeegan et al. (1985) and Fahey et al. (1987b). Nonlinear excesses in ^{26}Mg ($\delta^{26}\text{Mg}$ values) were calculated from the deviations ($\Delta^{25,26}\text{Mg}$ values in ‰) from the standard ratios (Catanzaro et al. 1966) under the assumption of a linear mass fractionation law (instrumental and intrinsic). Thus $\Delta^i\text{Mg} = 1000 \times ({}^iR_{\text{meas}}/{}^iR_{\text{stand}} - 1)$, where ${}^iR = ({}^i\text{Mg}/{}^{24}\text{Mg})$ for $i = 25, 26$, and $\delta^{26}\text{Mg} = \Delta^{26}\text{Mg} - 2 \times \Delta^{25}\text{Mg}$. Magnesium-Al measurements were made on various minerals in different locations in the inclusion as well as in the matrix outside of the inclusion. In addition, we measured Mg, Al, and Si isotopic compositions along two traverses (Fig. 2) from the exterior of the inclusion into the interior. With the exception of matrix points outside the CAI and one point on the rim in traverse #1, all spots were within melilite. We determined the intrinsic mass fractionations of Mg (from the $^{25}\text{Mg}/^{24}\text{Mg}$ ratio) and Si by normalizing the ratios measured inside the CAI to those determined for the matrix. The Mg ratios from the matrix agree well with those from terrestrial standards, and we assumed that the Si isotopic composition of the matrix matched terrestrial values.

Calcium and Ti isotopic measurements were made according to the techniques described by Zinner et al. (1986), Fahey et al. (1987a), and Ireland (1990).

Oxygen isotopic abundances were measured on a carbon-coated polished thin section with the UCLA Cameca IMS 1270 ion microprobe utilizing techniques similar to those described in McKeegan et al. (1998). Briefly, a mass-filtered, 20 keV, $\sim 0.5 \text{ nA}$ Cs^+ primary ion beam was used to sputter shallow ($< 2 \mu\text{m}$ deep) craters, $\sim 12 \mu\text{m}$ in longest dimension. Analyses were performed at high mass resolving power (~ 6000), sufficient to separate the O signals of interest from hydride mass interferences, and a normal-incidence electron flood gun was used for achieving charge compensation. A Faraday cup detector equipped with a Keithley 642 electrometer was used to measure the $^{16}\text{O}^-$ current, and the magnetic field was switched to sequentially measure secondary ion beams for the minor isotopes ^{17}O and ^{18}O by pulse counting with an electron multiplier. Corrections for background and deadtime were applied; both corrections are small under the analytical conditions and were made with high accuracy ($< \sim 0.1\%$). Data were corrected for instrumental mass fractionation (IMF) and relative detector efficiency by comparison to a Burma spinel standard (McKeegan 1987) measured intermittently with the White Angel. All results are reported relative to the standard mean ocean water (SMOW) scale. During one analytical session, additional analyses of a terrestrial quartz standard were made to check the accuracy of the detector yield calibration. The quartz data fall on the terrestrial mass

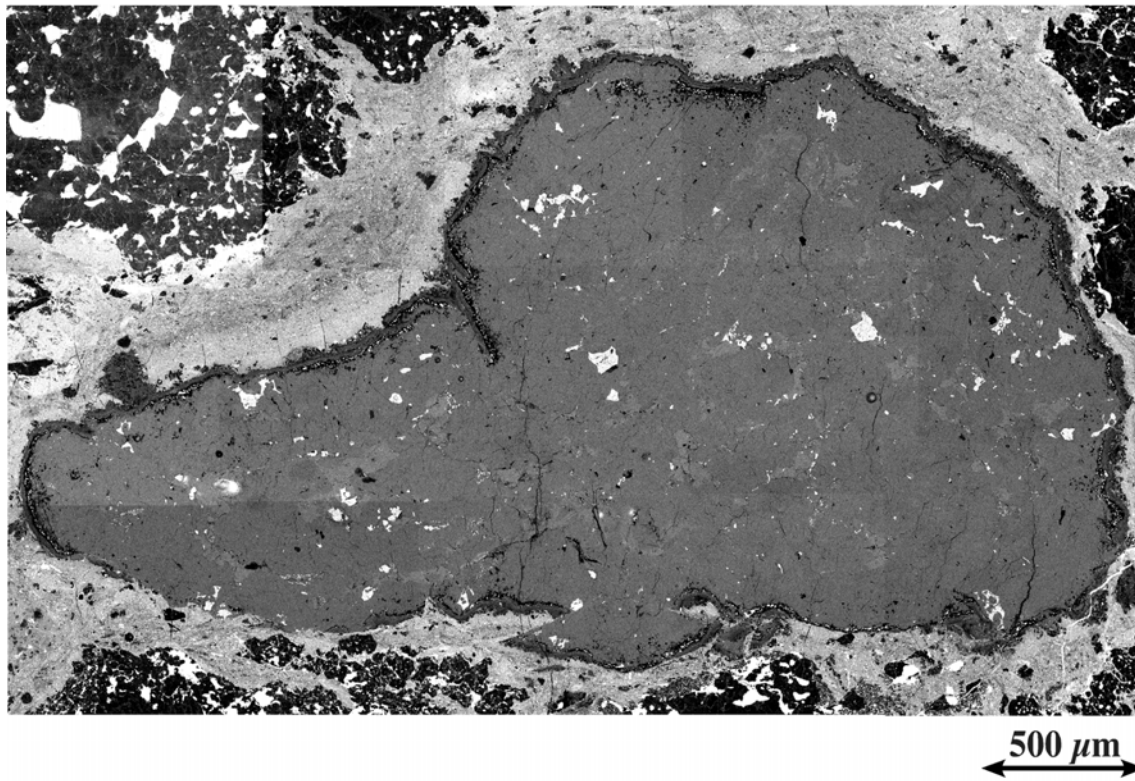


Fig. 1. Backscattered electron (BSE) microscope image of the Leoville White Angel refractory inclusion measuring 3.7 mm in length. Perovskite crystals are white. Melilite crystals are gray. Lighter gray areas are wollastonite crystals. Other mineral phases cannot be distinguished in this picture. Note that the rim is locally broken by microfaults.

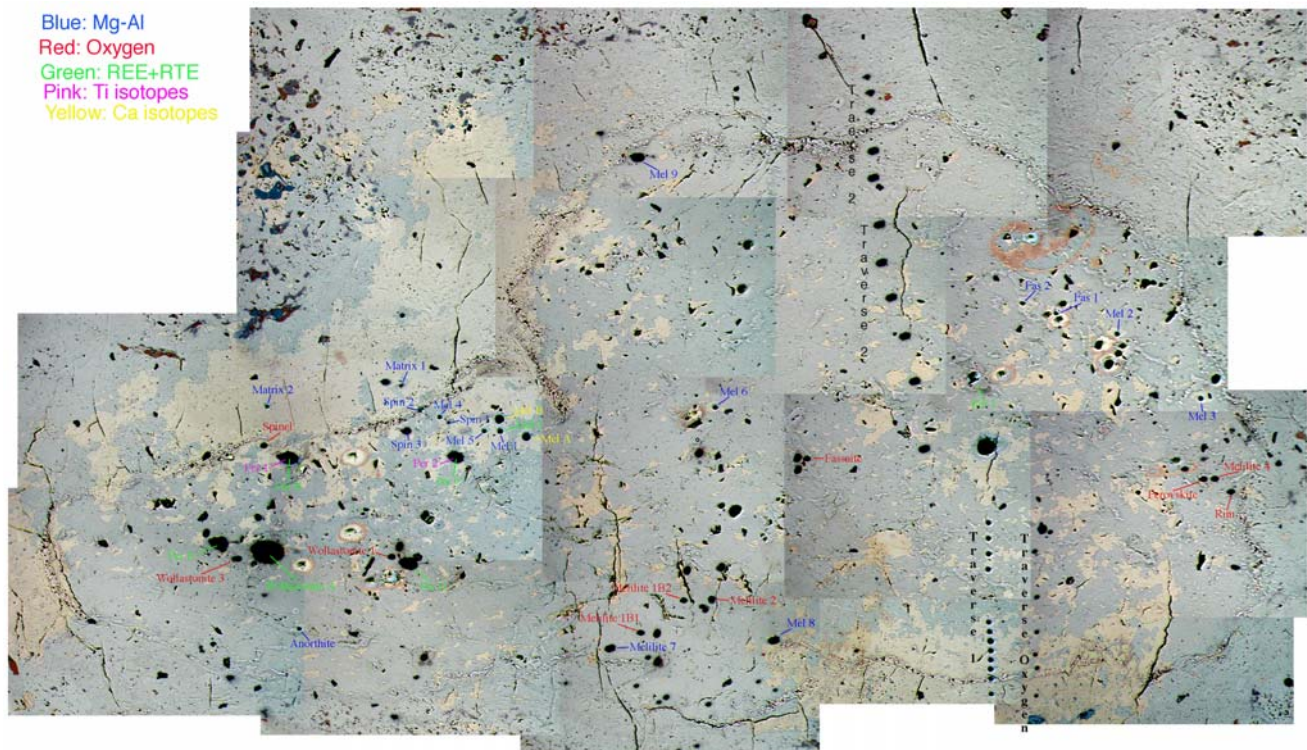


Fig. 2. Reflected light optical microscope photo showing isotopic measurement spots.

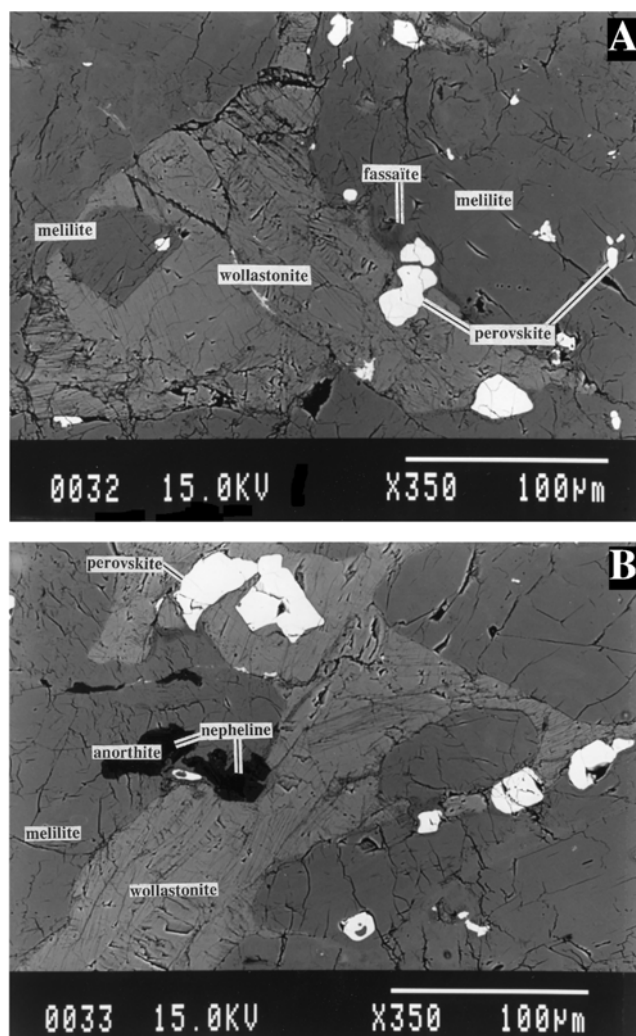


Fig. 3. a) and b) BSE photomicrographs of large equant wollastonite crystals in the core of the White Angel inclusion.

fractionation line within a precision of 0.8‰, and the average $\delta^{18}\text{O}$ agrees with the accepted value within 1.5‰. This result demonstrates that matrix effects on the instrumental mass fractionation correction between spinel and quartz is $<2\text{‰/amu}$, which is consistent with a large set of data obtained subsequent to the analyses reported in this work and indicates that, under our analytical conditions (i.e., low-energy secondary ions), silicate and oxide minerals that are relatively Fe-poor exhibit similar instrumental mass fractionation within $\sim 1\text{--}2\text{‰/amu}$ (e.g., Simon et al. 2000). For this reason, we are confident that we can utilize spinel as a standard for correction of IMF for all phases measured in the White Angel, including melilite, wollastonite, and perovskite, with an acceptable maximum systematic error of $\sim 2\text{‰/amu}$. This level of possible systematic error is commensurate with that arising from having the standards on a different physical mount than the sample thin section, and neither error is specifically accounted for in the final data

tabulation. The reported (1σ) uncertainties do include both the internal measurement precision for an individual analysis (typically $\sim 1\text{‰}$) and a measure of the external reproducibility on the spinel standard during a given analysis session (typical values ranged from ~ 0.5 to 1.5‰). Note that uncertainties in the magnitude of the correction for IMF have no influence on the determination of the deviation of any datum from the terrestrial mass fractionation line (expressed as $\Delta^{17}\text{O} = \delta^{17}\text{O} - 0.52 \delta^{18}\text{O}$). In addition to the oxygen isotopic analyses made on selected minerals, measurements were made on six melilite spots along a traverse parallel to the first traverse of Mg, Al, and Si measurements.

Trace Element Analyses

Trace element analyses were made both at Washington University and at Arizona State University with Cameca IMS 3F ion microprobes. The analyses at Washington University used a procedure modified from that of Zinner and Crozaz (1985). Relative ion yields for silicates are those given by Fahey et al. (1987b) and, for the other phases, those given by Ireland et al. (1991). Rare earth element (REE) analyses at ASU were made for a limited number of masses (138, 139, 140, 141, 143, 147, 151, 157, 159, 163, 165, 166, 169, 174, 175) plus mass 42 for Ca, which was used as a reference element. Analyses were made in two steps. First, the light REEs up to Eu (mass 151) were analyzed, with Ca being measured before and after, followed by the heavy REEs starting with Gd (mass 157), again flanked by Ca measurements. The energy bandpass was 40 eV, and the sample voltage was offset by -75 V relative to the centroid of the energy distribution. Charging was determined and compensated by monitoring the energy distribution for ^{42}Ca and changing the sample voltage offset. For a subset of spots, Sr, Y, Zr, and Nb were also measured. For the REE determinations, oxides of the light REEs were subtracted from the counts for the heavy REEs (Zinner and Crozaz 1986).

RESULTS

Petrography

The White Angel is an unusual, coarse-grained CAI from the Leoville CV3 chondrite (Figs. 1 and 2) that measures about 3.7×1.7 mm. It has a smooth shape and is surrounded by a regular and thin multilayer rim sequence. No core-mantle structure is evident. We named this inclusion “White Angel” because white minerals (wollastonite and melilite) represent more than $\sim 95\%$ of its volume. It can be classified as a compact type A inclusion (Grossman 1975) because it has a predominantly igneous texture and consists mainly of melilite (~ 84 vol%). Melilite crystals reach up to $600 \mu\text{m}$ in length

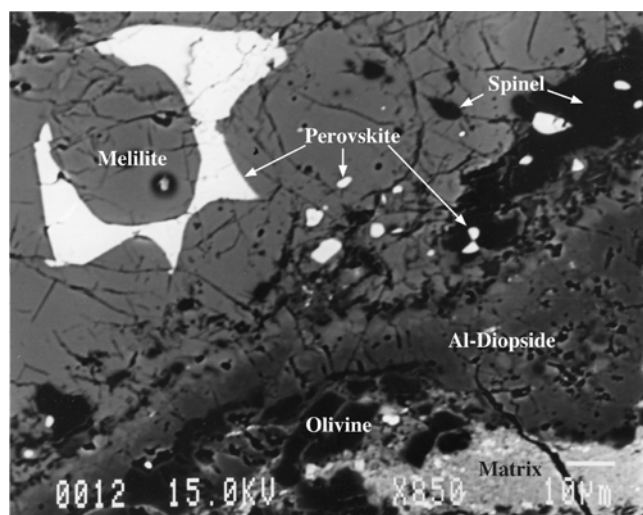


Fig. 4. BSE photomicrograph showing perovskite crystals growing between melilite crystals. A close-up of the rim of White Angel exhibits a layer of spinels, associated with small perovskite grains, parallel to an aluminous diopside layer and an outermost olivine layer.

and most appear to be randomly oriented, although some large crystals are oriented parallel to the lineation of the rock and show undulatory extinction and kink banding. However, the White Angel is distinct from typical type A CAIs (MacPherson et al. 1988; MacPherson 2003) in that it contains abundant (~12 vol%) large, equant wollastonite crystals throughout (in addition to minor fassaïte and perovskite). The occurrence of wollastonite as an igneous phase has not previously been reported in a refractory inclusion (Caillet and Buseck 1992). Allen et al. (1978) and Barber et al. (1984) described wollastonite needles in vugs of “fluffy” type A inclusions whose morphologies indicate direct condensation from a vapor. In contrast, the wollastonite crystals in the White Angel are massive (up to 400 µm long) (Figs. 3a and 3b) and in places they enclose perovskite grains. The wollastonite shows a pronounced blue-green luminescence under the electron beam. Like the melilite, some wollastonite crystals are flattened and show undulatory extinction and perfect cleavages characteristic of wollastonite.

Perovskite occurs throughout the CAI and constitutes about 3 vol%. Crystals vary in size between a few micrometers and 120 µm. Some are euhedral, but others occur in interstices between melilite crystals near the inclusion rim (Figs. 4 and 5). In places, perovskite is coated by a thin veneer of pyroxene. It also occurs as exsolution lamellae in fassaïte (Fig. 5) adjacent to wollastonite and larger pyroxene grains. The fassaïte and melilite appear to have been trapped during crystallization of perovskite (Fig. 6). Few micrometer-size grains of a niobate in perovskite and FeNi metal containing Ru, Ir and Pt, Rh, and Mo were found within a single crystal of melilite.

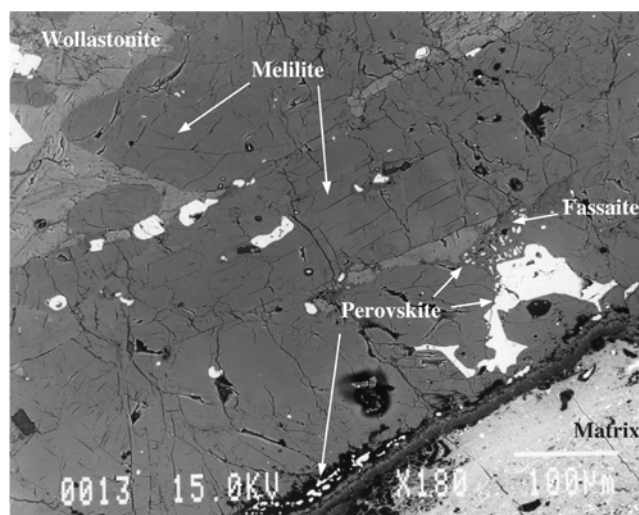


Fig. 5. BSE photomicrograph showing large melilite crystals, wollastonite (note the large area in the upper left corner), and perovskite. A probably late fassaïte-perovskite intergrowth is located next to wollastonite, melilite, and massive perovskite. The rim is in the lower right of the picture. The olivine layer was removed in some places.

Four large fassaïte crystals represent less than 1 vol% of the CAI. This Ti-rich pyroxene exhibits an intense green color, is pleochroic in transmitted light, and shows sector zoning.

The crystallization sequence, inferred from the textural relationships, is melilite, then perovskite and wollastonite, and finally fassaïte.

The White Angel also contains an accessory Ti-rich silicate, poikilitically enclosed in melilite (Fig. 7). It is reddish brown in plane light. In places it occurs next to fassaïte and as sparse hexagonal grains. The small size of the crystals (<10 µm) prevented X-ray diffraction characterization, however its composition is similar to the phase reported from an Essebi (CM2) CAI by El Goresy et al. (1984) and described by Paque et al. (1994) in synthetic and natural samples.

Spinel is absent from the CAI except near the rim. This distribution differs from typical type A inclusions, many of which contain between 15 to 20 vol% spinel (Grossman 1975). Like other Leoville inclusions, the White Angel lacks alkali-rich secondary minerals common in Allende inclusions. Only two small (up to 40 µm) anorthite crystals were found which are partially replaced by nepheline. However, some Ca-rich veins crosscut the inclusion and calcite fills cracks perpendicular to the long axis of the inclusion.

Although the overall texture indicates that the White Angel crystallized from a melt, some parts are brecciated and have features reminiscent of solid-state recrystallization. The inclusion displays several fracture planes characteristic of brittle deformation near and across the rim, a feature well

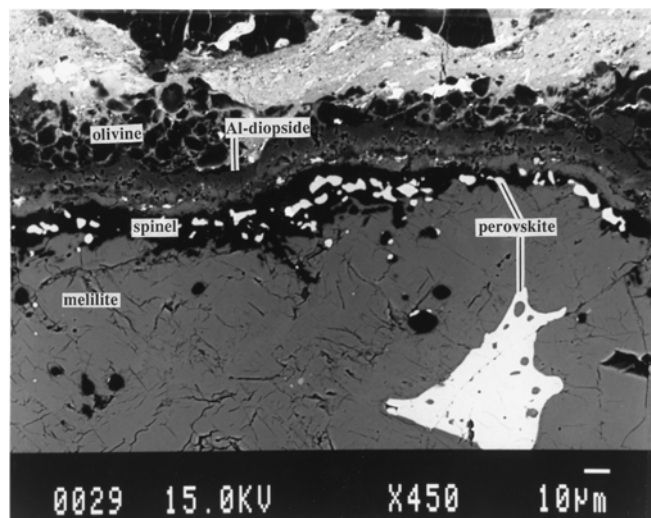


Fig. 6. BSE photomicrograph of the border of the White Angel inclusion. A large perovskite crystal has grown and trapped some melilite crystals (idiomorphic shapes as well as amoeboidal blebs). Note the regularity of the rimming sequence. The high albedo of the fine-grained matrix of Leoville is due to its enrichment in Fe, in contrast to the White Angel inclusion.

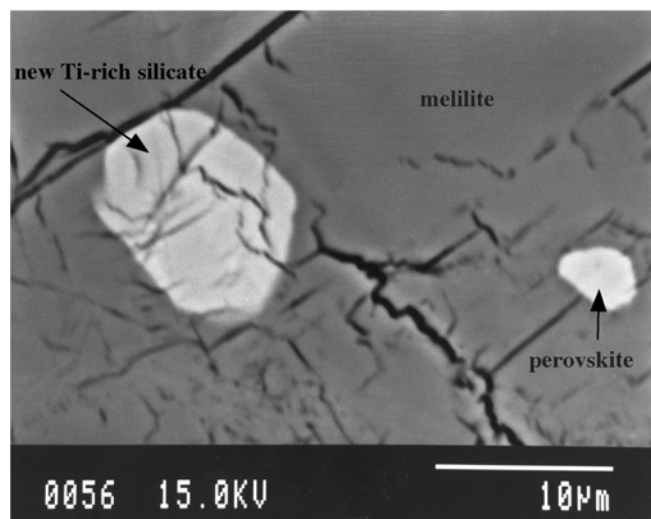


Fig. 7. BSE photomicrograph of the accessory Ti-rich silicate.

known in Leoville, Vigarano, and Efremovka CAIs (Cailliet et al. 1993; El Goresy et al. 2002). Two sets of faults indicate a direction of stress, perpendicular to the flattening direction of the CAI and the long axis of the CAI lies parallel to the direction of elongation of other components in Leoville. The rim is broken, sheared, abraded, and folded. Fe-rich opaque droplets in the matrix, which were mechanically emplaced by microfaults ("schlieren"?) into the inclusion, suggest that some local partial melting had occurred after accretion (Figs. 8a and 8b). Some topographic fractures extend into the matrix, indicating that they were probably generated during or after incorporation

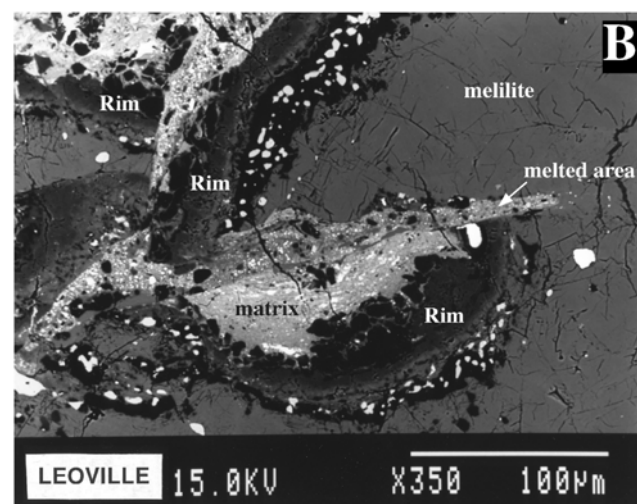
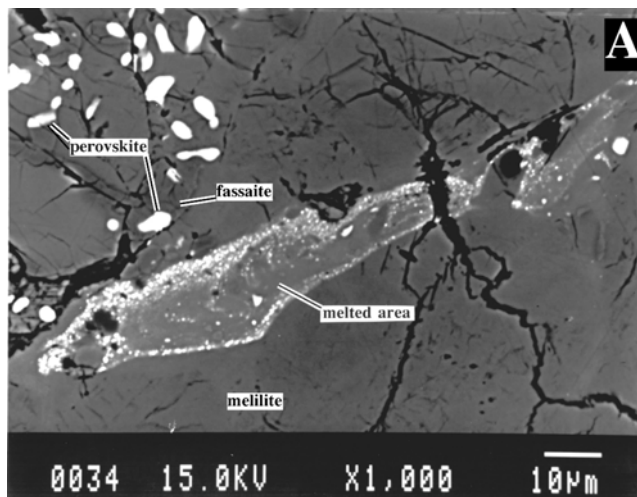


Fig. 8. a) and b) Plastically deformed regions of glass derived from melting of the meteorite matrix and partial melting of the inclusion intruded into fissure and fracture in the White Angel inclusion. Angular fragments of the CAI enclosed within the nearby matrix show no sign of melting or resorption.

of the White Angel into the Leoville parent body. Some calcite and accessory silica-rich patches (apparently replacing wollastonite) could also have preceded the faulting event(s) and therefore be preterrestrial.

The White Angel is surrounded by a rim (Figs. 4 and 6) of relatively constant thickness (30–50 μm). It consists, from the inside outward, of a spinel+perovskite layer, a thin gehlenite layer, in places decorated by sparse sulfide blebs, a thin porous irregular veneer of a silicate mineral (which could not be analyzed because of its small size) with high abundance of Al and Fe, possibly Fe-bearing Ti-rich pyroxene, the latter covered by a thicker regular aluminous diopside layer, and last an olivine layer. We found no alteration products such as grossular or sodalite. The first layer is continuous, unlike the other layers, which are absent in places. The olivine layer is

Table 1. Representative electron microprobe analyses of melilite from the White Angel.

	7	8	29	30	Average (179 analyses)	Range (min/max)
SiO ₂	22.16	26.44	30.29	31.77	26.99	(22.16–31.77)
TiO ₂	0.15	0.05	0.03	0.07	0.05	(bd–0.73)
Al ₂ O ₃	36.60	29.44	23.62	21.39	28.60	(21.39–36.60)
FeO	0.09	bd	bd	bd	0.05	(bd–0.54)
MgO	0.38	2.98	5.41	6.10	3.31	(0.38–6.10)
MnO	bd	bd	bd	bd		(bd–0.08)
CaO	40.37	40.10	41.32	41.50	40.72	(39.14–41.95)
K ₂ O	bd	bd	bd	bd		(bd–0.01)
Na ₂ O	bd	bd	0.04	0.13		(bd–0.18)
V ₂ O ₃	bd	bd	bd	bd		(bd–0.19)
Cr ₂ O ₃	bd	bd	bd	bd		(bd–0.04)
Total	99.75	99.02	100.71	100.99	99.75	
Number of cations per 14 oxygens						
Si	2.03	2.43	2.74	2.87	2.47	(2.03–2.87)
Ti	0.01					(0–0.05)
Al	3.94	3.19	2.52	2.27	3.08	(2.27–3.94)
Fe	0.01					(0–0.04)
Mg	0.05	0.41	0.73	0.82	0.45	(0.05–0.82)
Ca	3.95	3.95	4.01	4.01	3.99	(3.87–4.09)
Total	9.99	9.97	10.00	10.00	9.99	(9.95–10.04)
% Åk (Si,Al)	1	21	37	43	23.13	(1.35–43.23)

bd = below detection (detection limits in wt%: Na₂O = 0.013; K₂O = 0.014; FeO = 0.047; MnO = 0.05; V₂O₃ = 0.065; Cr₂O₃ = 0.023; TiO₂ = 0.02). Numbers in parentheses express compositional range.

sparse, and isolated olivine crystals in places form fluffy, thicker areas. The diopside layer is compact and does not contain isolated crystals.

Mineral Chemistry

Melilite

Representative analyses of melilites are listed in Table 1. Compositions range from Åk₁ to Åk₄₃ with an average of Åk₂₃ for 179 chemical analyses (Fig. 9). Crystals near the margin of the inclusion are more aluminous (gehlenitic). Almost pure gehlenite occurs close to the rim. Melilite has a low sodium content with Na₂O typically <0.1 wt%. Only eight analyses (less than 5% of all analyses) revealed Na₂O-contents between 0.05 and 0.18 wt% and there is no trend in the Na₂O content with increasing Åk content, consistent with results of Beckett and Stolper (2000) who showed that Na behaves as an incompatible element in gehlenitic melilite for melts with low Na₂O contents (<0.33 wt%). Melilite is generally more Mg-rich close to large wollastonite crystals and in the vicinity of deformed areas. The Fe content is generally below the detection limit (average of 0.05%), but local FeO enrichments with concentrations up to 0.54% occur toward the margin of the inclusion, perhaps because of local heating through parent body shock, particularly next to faults in the brecciated areas where partial melting occurred and the matrix is intermixed with the inclusion. Ranges of other minor elements in the melilites are TiO₂ up to 0.73% (average 0.05%); K₂O < 0.01%; V₂O₃ up to 0.19% (average 0.01%);

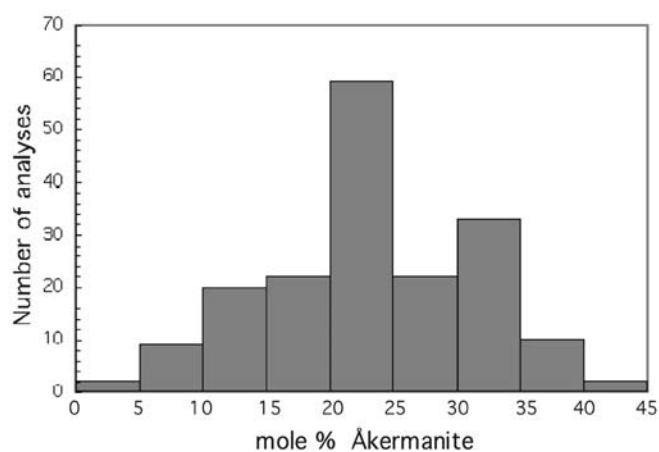


Fig. 9. Histogram of åkermanite contents of White Angel melilites. Two peaks can be distinguished. Melilite crystals with less than 10% Åk are located close to the rim of the inclusion.

Cr₂O₃ < 0.04%. The zoning is oscillatory in many places (Fig. 10).

Wollastonite

The composition of wollastonite is given in Table 2. There are no significant variations of the major elements among the stoichiometric analyses. Wollastonite contains minor amounts of TiO₂ (0.07–0.22 wt%; average 0.15 wt%), and the MgO content ranges from 0.53 to 0.75 wt%.

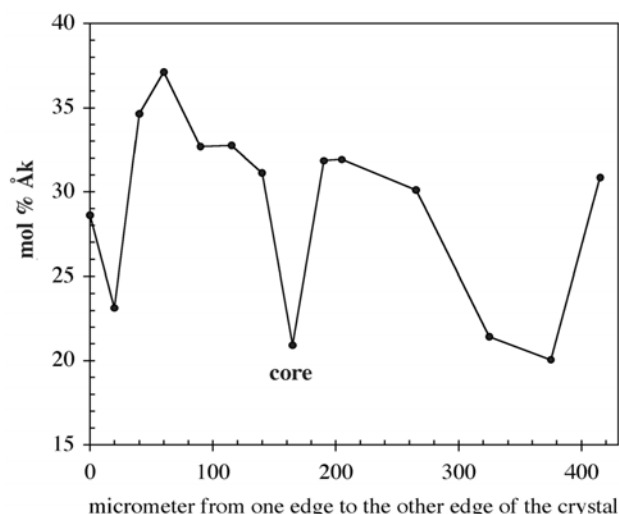


Fig. 10. Chemical composition profile across a typical melilite crystal. Zoning varies from åkermanite enrichment around an aluminous core, to evolve toward more gehlenitic compositions and then to revert back to more åkermanitic compositions at the edge of the crystal.

Fassaïte

Fassaïte in the White Angel (Table 3) contains very high concentrations of titanium, aluminum, and vanadium. TiO_2 (average: 17.55 wt%) ranges from 9.24 to 19.9 wt% in 52 analyses (Fig. 11). Eighty-five percent of the Ti is trivalent (calculated under the assumption of 4.0 cations) with $\text{Ti}^{3+}/(\text{Ti}^{3+}+\text{Ti}^{4+})$ lying between 0.63 and 0.99 (calculation by the method of Dowty and Clark 1973) (Fig. 12), which is quite high compared to the Ti^{3+} proportions in pyroxenes from type A or even type B inclusions reported in the literature (Simon et al. 1999). Al_2O_3 varies between 15.97 and 21.24% with an average of 19.42%. Ti and V are usually more enriched in the core of crystals. Some sector zoning is present with respect to Ti, V, and Al (Wass 1973). The V_2O_3 content is higher in Ti^{3+} -rich crystals that also exhibit strong green pleochroism (0.25–3.9%; average 1.71%) than in the rest of the fassaïte. The V_2O_3 content in small fassaïte crystals in contact with the unidentified Ti-rich silicate is systematically low compared to that in large crystals. The measured concentrations of minor elements are: FeO <0.09% (average 0.02%), MnO below 0.03%, Cr_2O_3 0–0.18% (average 0.09%). No compositional differences were detected between large fassaïte crystals and the thinner crystals associated with perovskite.

Perovskite

All perovskite crystals show very low concentrations of the oxides Nb_2O_5 , La_2O_3 , Ce_2O_3 , ThO_2 , Y_2O_3 , and ZrO_2 except one large crystal that shows a local enrichment in niobium, up to 5.31 wt%, suggesting the presence of a submicrometer niobate crystal (Table 4). Niobium replaces Ti

Table 2. Chemical composition of wollastonite in White Angel.

	10	Average (16 analyses)	Range (min/max)
SiO_2	51.49	51.91	(51.19–52.5)
TiO_2	0.25	0.15	(0.07–0.22)
Al_2O_3	0.06	0.03	(bd–0.06)
FeO	bd		(bd–0.08)
MgO	0.55	0.62	(0.53–0.75)
MnO	bd		(bd–0.06)
CaO	47.43	47.26	(45.98–48.55)
V_2O_3	bd	nd	
Cr_2O_3	bd	nd	
Nb_2O_5	bd	nd	
La_2O_3	bd	nd	
Ce_2O_3	0.08	nd	
ThO_2	bd	nd	
Total	99.90	100.01	(98.85–101.45)
Number of cations per 6 oxygens			
Si	1.99	2.00	
Ti	0.01	0.00	
Mg	0.03	0.04	
Ca	1.96	1.95	
Total	4.00	3.99	

nd = not detected; bd = below detection (detection limits in wt%: FeO = 0.047; MnO = 0.045; V_2O_3 = 0.07; Cr_2O_3 = 0.05; TiO_2 = 0.024).

Numbers in parentheses express compositional range.

in the chemical formula. Minor elements present are Si (0–0.72 wt%, but up to 0.92% in a small perovskite enclosed in pyroxene and 1.7% in intergrowth with fassaïte), Al (0.09–0.98 wt%, average 0.26 wt%), Mg (0–0.15 wt%, average 0.03 wt%; up to 0.88% in very small crystallites). Perovskite grains from the interior of the inclusion do not contain detectable Fe whereas the abundance of FeO reaches 0.32 wt% in one grain in the rim sequence of the inclusion. There are no other differences between the compositions of large perovskites and those in the fassaïte-perovskite within the rim layer associated with spinel. However, small silica contents could be attributed to contamination due to beam overlap of the small crystals in a host silicate.

Ti-Rich Silicate

We performed seven analyses of a Ti-rich silicate. The mineral contains 24.7–25.9% SiO_2 (average 25.48%), 26.5–28.2% TiO_2 (average 26.95%), 15.45–16.7% Al_2O_3 (average 16.07%) and 29.6–30.2% CaO (average 29.9%) corresponding to ranges observed in the mineral UNK (Paque et al. 1994). Na, K, Mn, Cr, Nb, La, Ce, and Th were not detected by electron microprobe and the FeO-content is below the detection limit. A formula composition, calculated on the basis of 14 oxygens, is $\text{Ca}_{2.94}\text{Ti}_{1.86}\text{Mg}_{0.04}\text{Al}_{1.74}\text{V}_{0.02}\text{Si}_{2.34}\text{O}_{14}$. Calcium constitutes a third of the cations. Ti^{3+} can be present because Ti+Si is in excess of 4 cations (11% would be trivalent).

Table 3. Representative electron microprobe analyses of fassaïte from White Angel.

	19 Large crystal	32 Around perovskite	20 Next to new mineral	Average (52 analyses)	Range (min/max)
SiO ₂	32.39	34.19	31.64	31.99	(30.1–36.9)
TiO ₂	17.66	15.01	17.76	17.55	(9.24–19.9)
Al ₂ O ₃	18.99	20.01	19.93	19.42	(15.97–21.24)
FeO	bd	0.06	0.05	bd	(bd–0.09)
MgO	5.50	7.03	6.37	5.45	(4.61–8.29)
MnO	bd	bd	0.06	bd	(bd–0.08)
CaO	23.79	24.68	23.90	24.02	(23.25–25.49)
K ₂ O	bd	bd	bd	bd	(bd–0.02)
Na ₂ O	bd	bd	bd	bd	(bd–0.03)
V ₂ O ₃	2.12	0.44	0.35	1.71	(0.25–3.9)
Cr ₂ O ₃	nd	nd	bd	0.09	(bd–0.18)
Total	100.46	101.45	100.10	100.27	(99.28–101.5)
Si	1.25	1.28	1.22	1.24	(1.17–1.39)
Ti ³⁺	0.46	0.32	0.38	0.44	(0.17–0.51)
Ti ⁴⁺	0.05	0.11	0.14	0.07	(0.01–0.16)
Al	0.87	0.89	0.90	0.89	(0.72–0.95)
Mg	0.32	0.39	0.37	0.31	(0.27–0.46)
Ca	0.99	0.99	0.98	1.00	(0.97–1.04)
V	0.07	0.01	0.01	0.05	(0.01–0.12)
Ti ³⁺ /Ti _{tot}	0.90	0.75	0.73	0.85	(0.63–0.99)

Ti³⁺ calculated assuming 4 cations per 6 oxygens.

bd = below detection (detection limits in wt%: Na₂O = 0.012; K₂O = 0.014; FeO = 0.047; MnO = 0.045; V₂O₃ = 0.07; Cr₂O₃ = 0.05; TiO₂ = 0.024).

nd = not detected.

Numbers in parentheses express compositional range.

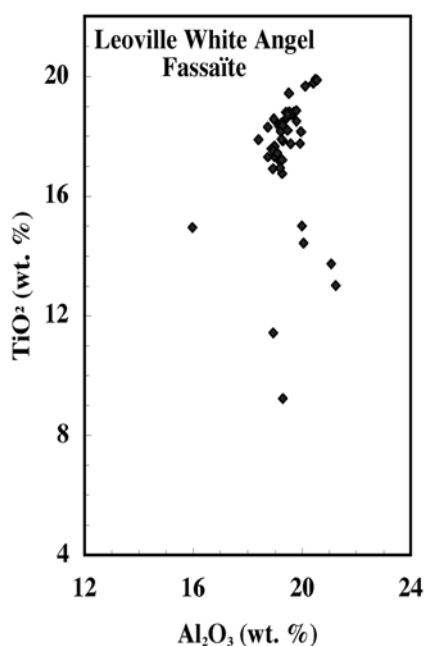


Fig. 11. TiO₂ versus Al₂O₃ in fassaïte crystals from Leoville White Angel.

Anorthite

Two central regions containing anorthite are partially altered to nepheline. Chemical analysis of one crystal gave the following concentrations: SiO₂ 42.59, TiO₂ 0.1, Al₂O₃

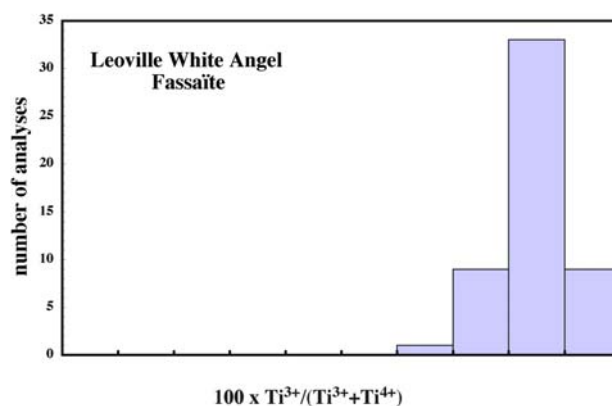


Fig. 12. Histogram of Ti³⁺ content for 52 analyses in White Angel fassaïte crystals.

36.45, FeO 0.03, MgO 0.13, MnO 0.03, CaO 18.76, K₂O 0.07, Na₂O 1.31, and V₂O₃ 0.07 (wt%).

Bulk Composition

The bulk chemical composition of the inclusion was determined by broad-beam electron microprobe analysis (Table 5) and compared with the composition obtained by multiplying the average compositions of each mineral species by its modal abundance. The composition is remarkable in

Table 4. Electron microprobe analyses of perovskite in White Angel.

Table 7. Electron microprobe analyses of perovskite in white fengite							
Large crystals				In the rim	In fassaïte	In wollastonite	In intergrowth
Average (18 analyses)							
Range (min/max)							
SiO ₂	0.20	(0–0.72)	0.04	0.15	0.92	0.06	1.70
TiO ₂	57.55	(55.88–58.75)	52.23	57.97	57.28	58.32	55.90
Al ₂ O ₃	0.22	(0.09–0.98)	0.81	0.45	0.40	0.17	0.42
FeO	bd	(0–0.32)	bd	0.12	bd	bd	0.06
MgO	0.03	(0–0.15)	bd	0.10	0.13	0.02	0.88
CaO	40.65	(39.42–41.37)	40.17	39.79	40.26	40.91	38.69
V ₂ O ₃	0.21	(0.09–0.4)	nd	nd	nd	nd	bd
Cr ₂ O ₃	bd	(bd–0.06)	nd	nd	nd	nd	bd
Nb ₂ O ₅	bd	(bd–0.09)	5.31	bd	bd	bd	nd
Total	98.93	(97.28–100.23)	98.62	98.69	99.06	99.56	97.76
Number of cations per 6 oxygens							
Si	0.01		0.00	0.01	0.04	0.00	0.08
Ti	1.98		1.82	1.99	1.96	1.99	1.92
Al	0.01		0.04	0.02	0.02	0.01	0.02
Mg	0.00		0.00	0.01	0.01	0.00	0.06
Ca	1.99		2.00	1.95	1.96	1.99	1.90
Nb	0.00		0.11	0.00	0.00	0.00	0.00
	4.00		3.98	3.99	3.99	4.00	3.98

bd = below detection (detection limits in wt%: FeO = 0.06; MgO = 0.01; MnO = 0.04; Cr₂O₃ = 0.05; V₂O₃ = 0.06; Nb₂O₅ = 0.1). All measurements for La₂O₃, Ce₂O₃, ThO₂, Y₂O₃, Sc₂O₃, ZrO₂, HfO, and MnO were under detection limits.

nd = not determined.

Numbers in parentheses express compositional range.

Table 5. Major element compositions (wt%) of the Leoville White Angel inclusion compared to CV3 refractory inclusions (MacPherson et al. 1988)

Inclusion	Type B1	Type B2	Type A	White Angel	
				Broad beam electron microprobe analyses (wt%)	Calculated compositions (B) from modal% of mineral phases ^a
SiO ₂	29.1	32.9	25.1	29.59	29.76
Al ₂ O ₃	29.6	26.7	37.6	24.65	23.93
TiO ₂	1.3	1.5	1.00	2.02	1.49
FeO	0.6	0.9	1.7	0.1	0.05
MgO	10.2	11.5	4.3	3.73	3.11
CaO	28.8	25.9	29.4	39.94	41.09
Na ₂ O	0.18	0.5	0.8	0.04	0.01
K ₂ O	0.01	0.02		0.01	
Cr ₂ O ₃	0.04	0.05	0.02	0.01	
MnO			0.01	0.02	0.01
V ₂ O ₃			0.09		0.03
NiO	0.06	0.04	0.03		nd
Sum	99.89	100.01	100.05	100.11	

^aPyroxene and the new mineral representing less than 1% of the mode are probably underestimated by this method.

terms of the very high Ca content compared to that of Al. The Ca/Al weight ratio is close to 2.3 and is hence much higher than the CI chondritic ratio of 0.75. This corresponds to 10% more Ca and 10% less Al than in type A refractory inclusions. Ti is also somewhat high and Mg is relatively low in concentration. If this composition was projected from spinel onto the An-Fo-Mel plane by the method of Stolper (1982), this composition would project close to the type A CAI field and melilite would be the liquidus phase. Additional

diagrams were designed later for CAIs having different compositions (Beckett and Stolper 1994; MacPherson and Huss 2005; Beckett et al. 2006) but they are also projections from spinel, which is the liquidus phase in most CAIs. However, this is not the case here and those diagrams are not appropriate for the White Angel. If one normalizes the bulk to a Mg- and Ti-free basis, the resulting composition plots in the melilite field in the system CaO-SiO₂-Al₂O₃ (Fig. 13). Accordingly, a liquid having this composition would

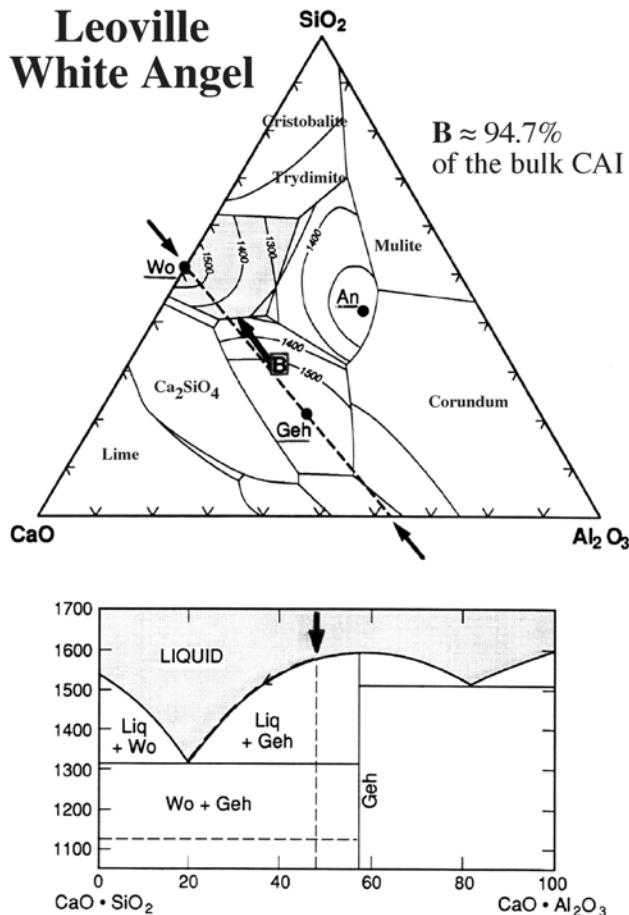


Fig. 13. Three-component system, Al_2O_3 - CaO - SiO_2 , showing boundary curves as solid lines, the stability fields of gehlenite (Geh), wollastonite (Wo), and anorthite (An), and other main fields, and the calculated bulk composition from Table 5 (B) of the White Angel inclusion based on just those three oxides. The binary diagram illustrates the evolutionary path of the melt upon cooling. It is clear that melilite is the liquidus phase and that wollastonite crystallizes from this melt. (Levin et al. 1964, p. 219).

crystallize melilite first, as observed in the White Angel, at about 1550 °C, and the remaining liquid would become enriched in CaO and SiO_2 until the temperature drops to about 1300 °C. At this temperature, wollastonite is expected to begin crystallizing along with melilite, consistent with our petrographic observations. Textural observations show clearly that perovskite crystallized before or along with wollastonite implying that significant TiO_2 was in the residual liquid following melilite crystallization (which is not accounted for in the phase diagram) and therefore that this diagram constitutes the only existing proxy for this phase assemblage.

Simon and Grossman (2004) calculate bulk CAI compositions by assuming chondritic Al/Ca ratios in type A and B inclusions and making corrections for observed ratios which can be biased because of radial heterogeneities in

Table 6. Electron microprobe analyses of mineral phases in the rim of the White Angel.

	Diopside	Spinel	Average (25 spinel analyses) Range (min/max)
SiO_2	54.93	0.07	(bd–0.41)
TiO_2	0.10	0.24	(0.15–0.35)
Al_2O_3	1.11	71.00	(69.65–72.29)
FeO	0.85	0.37	(bd–1.34)
MgO	17.71	27.73	(27.11–28.15)
MnO	bd	bd	
CaO	24.72	0.26	(0.08–0.81)
K_2O	0.02	nd	
Na_2O	0.06	nd	
V_2O_3	bd	0.46	(0.25–1.04)
Cr_2O_3	nd	0.14	(0.06–0.23)
ZnO	nd	bd	
Total	99.52	100.30	(99.17–101.54)
	Cations per 12 oxygens	Cations per 4 oxygens	
Si	3.98		
Ti	0.01		
Al	0.09	1.98	
Fe	0.05	0.01	
Mg	1.91	0.98	
Ca	1.92	0.01	
Na	0.01		
V		0.01	
	7.97	3.00	

bd = below detection (detection limits for spinel in wt%: MnO = 0.05;

ZnO = 0.1; SiO_2 = 0.01; Cr_2O_3 = 0.05; for diopside: see Table 3).

nd = not determined.

Numbers in parentheses express compositional range.

modal abundances. Although under or oversampling some minerals is certainly a problem for other type A (or type B) inclusions, this probably does not apply to the White Angel which lacks a core-mantle structure. Additionally, other evidence indicates that Al was apparently fractionated from Ca during the formation of the precursors of the inclusion by condensation from a gas depleted in highly refractory elements (see below).

Rim Sequence

The average chemical compositions of 25 spinels and of 2 diopside grains in the rim are given in Table 6. Spinel has low FeO contents of <1.34 wt% (average 0.37 wt%) with Cr_2O_3 varying from 0.06 to 0.23 wt% and MnO <0.05 wt%. V_2O_3 is more abundant, ranging from 0.25 to 1.04 wt%. The TiO_2 content varies between 0.15 and 0.35 wt%. No Zn was detected. Diopside contains up to 1.66 wt% Al_2O_3 and little TiO_2 . FeO reaches 1.12 wt% toward the margin of the inclusion next to the matrix. Other crystals could not be analyzed with accuracy due to their small size. However, only minor amounts of iron were detected in olivines from the outer layer of the rim.

Isotopic Compositions

The results of the Mg-Al isotopic measurements are given in Table 7. All phases inside the inclusion display isotopically heavy Mg with values for the fractionation ranging from 3.4 to 20.2‰/amu. As shown in Fig. 14, Mg mass fractionation varies systematically with distance from the rim of the CAI in a manner consistent with a diffusion profile. The fractionation is small close to the rim and reaches a more or less constant value at a distance of 200–300 μm toward the interior. The Mg isotopic fractionation inside the CAI is larger than that typical for “normal” inclusions, where it ranges to a maximum close to ~10‰, and is within the range observed in so-called FUN inclusions (Clayton et al. 1988). The melilite analysis points show nonlinear ^{26}Mg excesses that are well correlated with the $^{27}\text{Al}/^{24}\text{Mg}$ ratios (Fig. 15). A least-squares line fitted to all the data points except that for anorthite yields an inferred initial $^{26}\text{Al}/^{27}\text{Al}$ ratio of $(5.5 \pm 0.9) \times 10^{-5}$, with a reduced χ^2 of 0.86, within error identical to the “canonical” ratio found in most refractory inclusions (MacPherson et al. 1995) but also in agreement with recently measured “supra-canonical” ratios (Bizzarro et al. 2004, 2005; Young et al. 2005). In contrast, anorthite does not show any resolved ^{26}Mg excesses, in spite of a high $^{27}\text{Al}/^{24}\text{Mg}$ ratio of 728 (see Table 7), implying that the Mg isotopic composition in this mineral has been reset after most of the ^{26}Al had decayed or that anorthite is secondary. A 2σ upper limit on the inferred $^{26}\text{Al}/^{27}\text{Al}$ ratio is 4.4×10^{-6} , corresponding to a time difference of 2.6 Ma between CAI formation and isotopic resetting in anorthite.

Silicon isotopic ratios measured in the two traverses are shown in Table 8 and Si isotopic fractionation values are plotted in Fig. 16. Silicon is also isotopically heavy but the fractionation is much smaller than that for Mg. In contrast to Mg, there is no decrease in the fractionation close to the rim; and remarkably, the fractionation is largest right at the rim, but the error for this point is fairly large.

The oxygen isotopic data are given in Table 9 and plotted in Fig. 17. All data points lie on a line that is parallel to but slightly shifted toward the right of the carbonaceous chondrite anhydrous mineral (CCAM) mixing line (Clayton et al. 1977). This means that there is a large range of ^{16}O excesses among the minerals of the White Angel, but they all share approximately the same O-isotopic mass fractionation. The average value for this fractionation is $\text{Fo} = 5.5 \pm 0.5\text{‰/amu}$. The inferred ^{16}O excesses range from 8‰ to 48‰. Wollastonite shows the largest ^{16}O excess and melilite the smallest, whereas fassaite plots in between. Spinel grains in the CAI are quite small and the measurement point for the spinel extended into melilite. One measurement close to the rim was mostly on melilite but the beam spot included a tiny spinel grain. Perovskite has an O-isotopic composition close to that of melilite. It can be safely excluded that this is due to accidental beam overlap on melilite. The analysis spot on the perovskite grain could be clearly identified after the

measurement and was located completely inside the perovskite crystal. Two other measurements on perovskite grains are not included in the data set presented here (because of uncertainty about the exact magnitude of the O-isotopic fractionation) also yielded compositions close to that of melilite. The results of the measurements along the traverse and the spatial positions of the measurement points from the rim are included in Table 9 and Fig. 17. The data lie on the same mass-fractionated mixing line as all the other O-isotopic compositions measured in the inclusions and do not show any dependence of the O-isotopic fractionation on the distance from the rim. This is in clear contrast to the Mg isotopic fractionation (Fig. 14) that shows a systematic increase from the rim into the interior of the CAI.

Both Ca measured in melilite and Ti measured in perovskite show normal isotopic compositions within the analytical uncertainties. The results are plotted in Fig. 18 and compared with the Ca and Ti isotopic compositions of the FUN inclusions EK1-4-1, C1, and HAL, which all have large isotopic anomalies (Lee 1988). The White Angel is apparently only an F and not a FUN inclusion, similar to Allende inclusion TE that has large mass dependant fractionations in Mg and O (Clayton et al. 1984; El Goresy et al. 1991) but isotopically normal Ca and Ti.

Trace Element Abundances

The trace element abundance data are reported in Tables 10 and 11 and Figs. 19 and 20. Table 10 gives the concentrations of trace elements measured with the Washington University ion probe on melilite, wollastonite, and five perovskite grains. Most of these data, normalized to chondritic abundances (Anders and Grevesse 1989), are plotted in Fig. 19. Table 11 contains the average trace element concentrations measured at the Arizona State University ion probe on melilite (11 points), wollastonite (5 points), fassaite (7 points), and perovskite (5 points). The averaged CI-normalized REE abundances of all measurements for the minerals in which trace elements were analyzed are plotted in Fig. 20 together with the REE pattern for the whole inclusion obtained from individual mineral patterns and the modal abundances of the minerals. The whole inclusion has an REE pattern depleted in the ultrarefractory (UR) elements and enriched in the relatively volatile elements Eu and Yb (Fegley and Ireland 1991; see also Kimura et al. 1993 and Weber et al. 1995). It is essentially the inverse of an ultrarefractory pattern such as, for example, that exhibited by the Efremovka inclusion 101.1 (El Goresy et al. 2002). This group II-related pattern left its imprint upon all the analyzed mineral phases.

DISCUSSION

The White Angel is a unique compact type A (CTA) inclusion because it contains large wollastonite crystals

Table 7. Mg isotopic data.

Mineral	Distance from rim (μm)	$\Delta^{25}\text{Mg}$ (‰) $\pm 2\sigma$	$\Delta^{26}\text{Mg}$ (‰) $\pm 2\sigma$	F_{Mg} (‰) $\pm 2\sigma$	$\delta^{26}\text{Mg}$ (‰) $\pm 2\sigma$	$^{27}\text{Al}/^{24}\text{Mg}$
Spinel						
Spot 1	78	-4.4 ± 1.9	-7.2 ± 1.1	8.5 ± 2.0	1.6 ± 3.4	3.74 ± 0.02
Spot 2	0	-13.7 ± 1.6	-27.1 ± 1.4	-0.8 ± 1.6	0.2 ± 2.9	3.43 ± 0.08
Spot 3	30	-4.7 ± 0.4	-8.4 ± 0.5	7.0 ± 0.4	1.0 ± 0.9	3.82 ± 0.10
Fassaite						
Spot 1	344	7.3 ± 1.6	15.4 ± 1.8	20.2 ± 1.6	0.9 ± 2.8	4.2 ± 0.1
Spot 2	311	5.9 ± 1.3	12.7 ± 1.6	18.8 ± 1.2	0.9 ± 2.4	5.3 ± 0.4
Melilite						
Spot 1	184	-0.6 ± 1.7	3.7 ± 2.0	12.3 ± 1.8	4.9 ± 2.8	11.9 ± 0.1
Spot 2	206	0.1 ± 1.5	4.3 ± 1.8	13.0 ± 1.6	4.0 ± 2.9	11.8 ± 0.1
Spot 3	78	-3.8 ± 1.6	-4.5 ± 1.9	9.1 ± 1.6	3.0 ± 2.9	9.8 ± 0.1
Spot 4	45	-5.6 ± 1.6	-9.6 ± 1.6	7.3 ± 1.6	1.6 ± 2.7	10.5 ± 0.2
Spot 5	145	0.4 ± 1.3	2.7 ± 1.7	13.3 ± 1.4	2.0 ± 3.2	10.2 ± 0.1
Spot 6	800	0.1 ± 1.2	2.5 ± 1.4	13.0 ± 1.2	2.3 ± 2.1	9.2 ± 0.1
Spot 7	22	-8.9 ± 0.8	-12.3 ± 1.0	2.8 ± 0.8	5.6 ± 1.9	15.9 ± 0.1
Spot 8	35	-4.7 ± 0.8	-4.3 ± 1.1	7.0 ± 0.8	5.0 ± 1.3	9.2 ± 0.1
Spot 9	22	-8.3 ± 1.1	-10.1 ± 1.1	3.4 ± 1.1	6.6 ± 1.7	17.4 ± 0.7
Anorthite						
Spot 1		-2.1 ± 10.3	-1.1 ± 9.4	9.6 ± 10.3	3.2 ± 19.7	728 ± 81
Matrix						
Spot 1	-110	-12.1 ± 0.6	-24.6 ± 0.7	0.8 ± 0.6	-0.5 ± 1.0	0.13 ± 0.2
Spot 2	-55	-13.4 ± 0.7	-26.5 ± 0.8	-0.5 ± 0.7	0.1 ± 0.9	0.14 ± 0.14
Traverse #1						
Spot 1	-100	-10.5 ± 1.0	-22.7 ± 0.9	1.9 ± 1.0	-1.6 ± 2.3	0.16 ± 0.3
Spot 2	-50	-11.8 ± 1.1	-25.5 ± 1.4	0.5 ± 1.1	-1.8 ± 2.4	0.15 ± 0.28
Spot 3	0	-13.7 ± 1.2	-29.3 ± 0.9	-1.3 ± 1.2	-2.0 ± 2.5	3.4 ± 0.1
Spot 4	30	-8.2 ± 3.0	-12.0 ± 2.3	4.2 ± 3.0	4.4 ± 6.4	13.7 ± 0.3
Spot 5	60	-6.2 ± 2.3	-9.9 ± 2.7	6.2 ± 2.3	2.5 ± 5.4	8.7 ± 0.2
Spot 6	90	-4.2 ± 2.2	-4.2 ± 2.1	8.2 ± 2.2	4.2 ± 4.8	12.8 ± 0.2
Spot 7	120	-3.4 ± 1.9	-4.0 ± 1.8	9.0 ± 1.9	2.8 ± 4.2	10.8 ± 0.3
Spot 8	150	-3.7 ± 2.0	-2.5 ± 1.8	8.7 ± 2.0	4.9 ± 4.3	7.3 ± 0.2
Spot 9	180	-2.5 ± 1.6	-2.5 ± 1.8	9.9 ± 1.6	2.5 ± 3.6	5.1 ± 0.1
Spot 10	348	0.8 ± 5.8	7.1 ± 4.5	13.2 ± 5.8	5.5 ± 12.5	12.6 ± 0.2
Spot 11	400	2.7 ± 2.0	7.7 ± 2.2	15.1 ± 2.0	2.2 ± 4.6	10.3 ± 0.3
Spot 12	450	4.8 ± 2.3	10.2 ± 2.8	17.2 ± 2.3	0.7 ± 5.3	9.7 ± 0.1
Spot 13	500	0.6 ± 2.0	7.5 ± 2.6	13.0 ± 2.0	6.4 ± 4.7	10.3 ± 0.2
Traverse #2						
Spot 1	-125	-11.7 ± 0.9	-23.4 ± 0.8	-0.0 ± 0.9	0.1 ± 1.9	0.12 ± 0.02
Spot 2	-64	-11.7 ± 0.6	-23.5 ± 0.6	0.0 ± 0.6	-0.1 ± 1.3	0.15 ± 0.02
Spot 3	65	0.6 ± 1.8	2.3 ± 1.4	12.3 ± 1.8	1.2 ± 3.9	7.2 ± 0.2
Spot 4	149	2.6 ± 1.4	8.6 ± 2.0	14.3 ± 1.4	3.4 ± 3.5	11.2 ± 0.2
Spot 5	298	4.5 ± 1.2	10.0 ± 1.2	16.2 ± 1.2	1.1 ± 2.8	8.1 ± 0.1
Spot 6	421	3.7 ± 1.5	11.3 ± 1.5	15.4 ± 1.5	3.9 ± 3.3	12.2 ± 0.2
Spot 7	538	2.4 ± 1.6	8.6 ± 1.4	14.1 ± 1.6	3.8 ± 3.5	11.4 ± 0.1
Spot 8	671	2.7 ± 1.6	10.6 ± 1.4	14.4 ± 1.6	5.2 ± 3.5	11.1 ± 0.3
Spot 9	818	3.0 ± 1.3	10.5 ± 1.5	14.7 ± 1.3	4.5 ± 2.9	7.8 ± 0.2
Spot 10	1036	2.5 ± 0.8	7.9 ± 1.7	14.2 ± 1.1	2.9 ± 2.1	5.5 ± 0.1

representing about 12 vol% of the whole inclusion. This mineral is absent as a primary phase from the list of minerals given by Brearley and Jones (1998) observed in CAIs. In fact, wollastonite is not predicted to be a stable nebular condensate and until the present study it has never been encountered as

large crystals within CAIs. If it condensed, it must have done so when nebular melting and recrystallization of CAIs had largely ceased, below 1000 K. This apparently was the case for wollastonite needles occurring in vugs in compact type A or around fluffy type A inclusions (Allen et al. 1978). In these

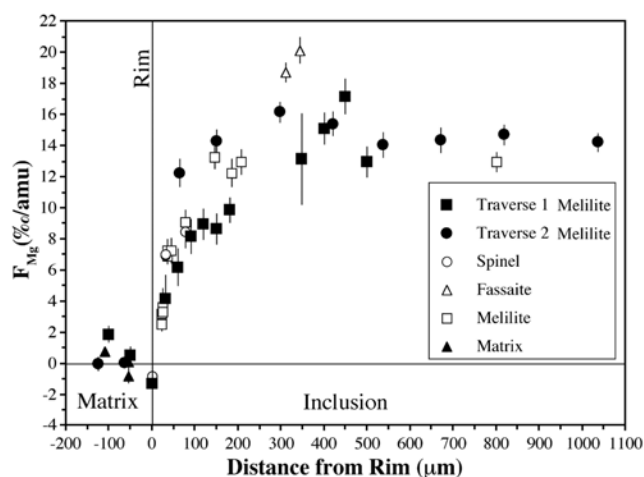


Fig. 14. The Mg isotopic mass fractionation (determined from the $^{25}\text{Mg}/^{24}\text{Mg}$ ratios) in the White Angel inclusion is plotted as a function of distance from the rim of the CAI. The large fractionation in the interior indicates evaporation of Mg from a melt. The gradient toward the border indicates subsequent partial equilibration with isotopically normal Mg.

cases it is clearly secondary in origin and formed after CAI crystallization.

CTA inclusions are extremely melilite-rich (up to 90 vol%) with moderate amounts of spinel and minor fassaite and perovskite. However, the White Angel is not only unusual in terms of its mineralogy (large amount of coarse-grained wollastonite and very few spinel crystals), it also has a superchondritic bulk Ca/Al ratio (~ 2.3). This means that it cannot be a residue of volatilization of precursors with chondritic composition because CaO is more volatile than Al_2O_3 . This ratio is much higher than any found in type A or type B inclusions. However, the Mg isotopic fractionation shows that the inclusion lost Mg by evaporation while molten (see below). Therefore the precursors already had a very unusual elemental composition to start with.

The White Angel shows the inverse of an ultrarefractory REE abundance pattern with large positive Eu, Yb anomalies. This is similar to a group II REE abundance pattern indicating that the CAI formed by condensation of precursors from a gas that was already depleted in the most refractory REEs (Boynton 1975). This gas must have also been depleted in Al, resulting in the low Al/Ca ratio of the inclusion. On the other hand, the oxygen, magnesium, and silicon isotopes do not show a condensation signature, but rather indicate mass loss by evaporation. The normal Ca and Ti isotopic ratios and the canonical initial $^{27}\text{Al}/^{26}\text{Al}$ ratio demonstrate that the White Angel is not a FUN inclusion but it can be considered as an “F” (fractionated) inclusion, similar in some respects to the TE inclusion reported by Clayton et al. (1984), Niederer and Papanastassiou (1984), and Niederer et al. (1985).

Finally, the layers of the rim sequence maintain a remarkably consistent thickness around the inclusion (Wark

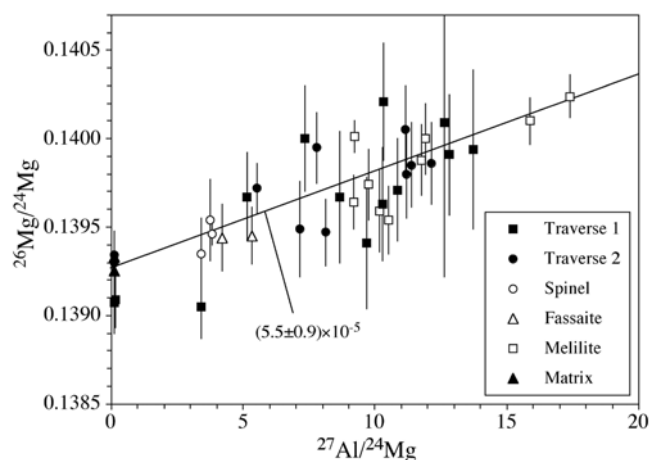


Fig. 15. The $^{26}\text{Mg}/^{24}\text{Mg}$, after correction for mass-dependent isotopic fractionation, is plotted against the $^{27}\text{Al}/^{24}\text{Mg}$ ratio. The slope of the correlation line indicates an initial $^{26}\text{Al}/^{27}\text{Al}$ ratio of $(5.5 \pm 0.9) \times 10^{-5}$, within the errors indistinguishable from the “canonical” ratio found in many CAIs.

and Lovering 1977; Wark and Boynton 2001). The rim is broken and fractured together with the CAI interior in many places, indicating that it formed before accretion and was disturbed within the Leoville matrix during the main shock that affected its parent body.

Formation Conditions: Insights from Petrography, Mineral Chemistry, and Bulk Composition

The coarse-grained melilite crystals in the White Angel exhibit complex oscillatory zoning with reverse-zoning evident over restricted portions of individual crystals. Reverse zoning is typically seen in type B CAIs due to the coprecipitation of fassaite, which lowers the Mg/Al ratio of the residual liquid (MacPherson et al. 1984). It has also been observed in Allende CTAs by Simon et al. (1999). In contrast to most type A CAIs, the melilite crystals in the White Angel have cores enriched in gehlenite, indicating crystallization at high temperature, followed by enrichment in the åkermanite molecule, characteristic of lower temperatures, as normally expected for an igneous zoning. However, this trend inverts near the edges, a feature we explain in terms of the onset of crystallization of wollastonite (Fig. 13). Wollastonite crystallization results in a decrease in the Si content of the melt, thereby enriching melilite in the gehlenite component which is Si-poor relative to åkermanite. The phase diagram allows for co-crystallization of wollastonite+gehlenite. In addition, crystals at the border of the inclusion are more refractory and show increases in Åk contents from the outer edges inward. However, some grains of melilite, and wollastonite as well, have a brecciated appearance and were highly strained as seen in other Leoville refractory inclusions (Cailliet et al. 1993), which makes the zonation look occasionally more complex. In some cases the long axis of

Table 8. Si isotopic data.

Spot	Distance from rim (μm)	$\Delta^{29}\text{Si}$ (‰) $\pm 2\sigma$	$\Delta^{30}\text{Si}$ (‰) $\pm 2\sigma$	F^{29}_{Si} (‰) $\pm 2\sigma$	F^{30}_{Si} (‰) $\pm 2\sigma$
Traverse #1					
Spot 1	-100	-44.6 ± 2.0	-84.8 ± 1.9	0.7 ± 2.5	0.5 ± 1.3
Spot 2	-50	-46.0 ± 2.0	-87.1 ± 2.9	-0.7 ± 2.5	-0.7 ± 1.6
Spot 3	0	-37.3 ± 4.9	-69.0 ± 6.7	8.0 ± 5.1	8.3 ± 3.4
Spot 4	30	-38.0 ± 3.4	-79.6 ± 2.7	7.3 ± 3.7	3.1 ± 1.6
Spot 5	60	-41.8 ± 2.8	-80.4 ± 2.7	3.5 ± 3.1	2.7 ± 1.6
Spot 6	90	-40.2 ± 2.8	-75.6 ± 3.5	5.2 ± 3.1	5.1 ± 1.9
Spot 7	120	-41.9 ± 3.2	-78.1 ± 2.5	3.4 ± 3.5	3.8 ± 1.5
Spot 8	150	-39.7 ± 2.5	-78.5 ± 2.4	5.6 ± 2.9	3.6 ± 1.5
Spot 9	180	-38.3 ± 3.4	-76.0 ± 2.7	7.0 ± 3.7	4.9 ± 1.6
Spot 10	348	-40.1 ± 4.4	-80.9 ± 2.8	5.2 ± 4.7	2.4 ± 1.6
Spot 11	400	-42.7 ± 2.8	-78.2 ± 2.4	2.6 ± 3.2	3.8 ± 1.5
Spot 12	450	-38.7 ± 2.6	-77.3 ± 3.1	6.6 ± 3.0	4.2 ± 1.8
Spot 13	500	-37.7 ± 2.8	-76.7 ± 2.5	7.6 ± 3.1	4.5 ± 1.5
Traverse #2					
Spot 1	-125	-46.3 ± 1.9	-89.6 ± 2.6	0.6 ± 2.3	-0.3 ± 1.5
Spot 2	-64	-47.4 ± 1.9	-88.5 ± 1.9	-0.6 ± 2.3	0.2 ± 1.2
Spot 3	65	-43.7 ± 2.4	-82.0 ± 2.1	3.1 ± 2.7	3.5 ± 1.3
Spot 4	149	-43.5 ± 2.1	-83.0 ± 2.0	3.4 ± 2.5	3.0 ± 1.2
Spot 5	298	-43.2 ± 2.0	-83.8 ± 1.8	3.7 ± 2.4	2.6 ± 1.2
Spot 6	421	-43.0 ± 2.0	-84.3 ± 2.5	3.9 ± 2.4	2.4 ± 1.5
Spot 7	538	-42.9 ± 2.4	-81.7 ± 2.1	4.0 ± 2.7	3.6 ± 1.3
Spot 8	671	-43.9 ± 2.0	-85.5 ± 1.9	3.0 ± 2.4	1.8 ± 1.2
Spot 9	818	-43.2 ± 2.5	-86.2 ± 2.3	3.7 ± 2.8	1.4 ± 1.4
Spot 10	1036	-43.8 ± 1.9	-82.7 ± 1.8	3.1 ± 2.3	3.1 ± 1.2

melilite crystals even lies parallel to the lineation of the meteorite, and no axiolitic texture can be easily recognized at the outer edge of the inclusion.

Fassaite crystals have cores that are enriched in both Ti and Al relative to their rims, with less variation in Al than in Ti. The cores, which have intense green color in transmitted light, exhibit large enrichments in Ti^{3+} relative to Ti^{4+} resulting from formation in highly reducing conditions (Beckett and Grossman 1986). Beckett (1986) showed experimentally that the calculated $\text{Ti}^{3+}/\text{Ti}^{4+}$ ratios of the meteoritic type B1 pyroxenes imply reducing environments for CAI formation, with $\log f\text{O}_2 = -19.5$, which is a factor of 100 to 1000 times more reducing than a solar gas at 1500 K. In the White Angel, the clinopyroxene crystals contain up to almost 20 wt% TiO_2 and very high $\text{Ti}^{3+}/\text{Ti}^{4+}$ ratios, which indicate even more reducing conditions. However, it has been noted by Beckett (1986) that high $\text{Ti}^{3+}/\text{Ti}^{4+}$ ratios could also reflect the preference of growing fassaite crystals for Ti^{3+} over Ti^{4+} . If all perovskite would have crystallized before fassaite, it could have resulted in a strong increase in the concentration of Ti^{3+} relative to Ti^{4+} in the liquid. The fassaite crystals in the White Angel exhibit sector zoning, which is compatible with crystallization from a melt. (This reflects the ability of clinopyroxene to grow parallel to more than one crystallographic plane.) The growth rate of fassaite relative to the diffusion rate in the residual liquid of the White Angel was therefore rapid (Simon and Grossman 2006). Idiomorphic

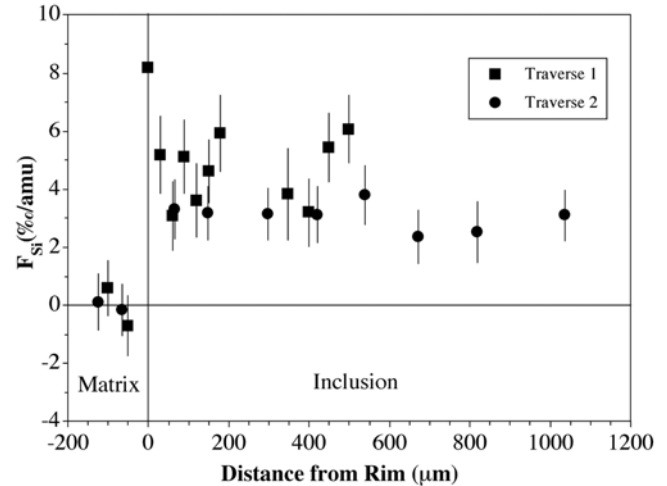


Fig. 16. The Si isotopic mass fractionation is plotted as a function of distance from the rim of the inclusion. In contrast to the Mg fractionation (Fig. 14), no gradual decrease to a normal composition is seen close to the border.

crystals of melilite also indicate rapid growth of perovskite in the liquid, trapping some melilite.

Perovskite is not expected to appear early in the equilibrium crystallization sequences of the White Angel melt as it is for most of the CAIs depleted in Ti. In the White Angel, the bulk Ti content is a little higher than in most type

Table 9. Oxygen isotopic data.

Mineral	$\delta^{17}\text{O}$ (‰) $\pm 2\sigma$	$\delta^{18}\text{O}$ (‰) $\pm 2\sigma$	$\Delta^{17}\text{O}$ (‰) $\pm 2\sigma$	^{16}O excess (‰)	Distance from rim
San Carlos standard	2.0 \pm 2.4	5.4 \pm 2.7	-0.8 \pm 2.8	1.6	
	2.3 \pm 2.7	3.5 \pm 2.5	0.5 \pm 3.0	-1.1	
	1.6 \pm 2.9	5.6 \pm 2.8	-1.3 \pm 3.3	2.7	
	1.6 \pm 3.5	3.6 \pm 3.2	-0.3 \pm 3.8	0.6	
Melilite	1.8 \pm 2.4	12.7 \pm 2.3	-4.7 \pm 2.7	9.7	
	1.8 \pm 3.0	11.7 \pm 3.0	-4.3 \pm 3.4	8.9	
	2.7 \pm 2.6	12.1 \pm 2.7	-3.6 \pm 2.9	7.5	
	0.3 \pm 2.6	10.5 \pm 2.7	-5.2 \pm 3.0	10.7	
	-0.3 \pm 2.7	10.4 \pm 2.4	-5.7 \pm 3.0	11.8	
	-2.8 \pm 2.9	6.7 \pm 2.5	-6.3 \pm 3.2	13.1	
Spinel	-8.3 \pm 3.0	2.6 \pm 2.2	-9.6 \pm 3.2	20.0	
Perovskite	1.0 \pm 2.3	9.2 \pm 2.1	-3.7 \pm 2.5	7.8	
Fassaïte	-17.7 \pm 2.3	-9.8 \pm 2.5	-12.6 \pm 2.7	26.3	
Wollastonite	-40.7 \pm 2.7	-34.1 \pm 2.5	-23.0 \pm 3.0	47.9	
	-40.9 \pm 2.3		-22.9 \pm 2.6	47.7	
Burma spinel standard	12.4 \pm 7		1.0 \pm 1.9		
	12.0 \pm 2.2		-0.3 \pm 2.6		
	12.2 \pm 2.2		0.4 \pm 2.4		
	10.0 \pm 1.6		-0.3 \pm 1.8		
	11.6 \pm 1.9		-0.3 \pm 2.1		
	10.9 \pm 2.0		-0.1 \pm 2.2		
	12.6 \pm 1.4		0.6 \pm 1.6		
Traverse					μm
Spot 1	5.2 \pm 2.7		-2.2 \pm 2.4	4.5	30
Spot 2	3.5 \pm 2.2		-2.8 \pm 1.7	5.8	70
Spot 3	5.7 \pm 2.6		-2.8 \pm 2.3	5.9	135
Spot 4	4.0 \pm 2.7		-2.9 \pm 2.4	6.0	235
Spot 5	6.5 \pm 2.5		-1.3 \pm 2.3	2.7	375
Spot 6	3.8 \pm 2.8		-3.4 \pm 2.7	7.1	425

A inclusions (see Table 5) and perovskite appears to have followed melilite. Some of the large perovskite crystals evidently grew before other mineral phases in the inclusion. All perovskite grains (large grains, grains intergrown with the late fassaïte, and small grains), have almost identical trace element contents across the whole inclusion, indicating that they were cogenetic (El Goresy et al. 2002). Most of the concentrations of these trace elements are below the detection limits of the electron microprobe. However, ion microprobe analyses of perovskites show that they do contain small amounts of Y, Zr, and to a lesser extent, Sc, up to about 10 times chondritic abundances. Symplectite existence is another piece of evidence that perovskite-fassaïte crystallized from a late, Ti-rich liquid (El Goresy et al. 1977). This feature is in agreement with a rapid crystallization process.

No metal grains were found that would suggest possible reduction after formation. Moreover, the restricted anorthite area grew late because of its lobate shapes obviously replacing melilite and its lack of excess ^{26}Mg .

We know that equilibrium condensation calculations predict that melilite condensed before spinel (Ebel and

Grossman 2000). However, textures and mineral chemistry indicate that the White Angel crystallized from a melt. The bulk compositions of most CAIs are consistent with Al-Mg spinel as the liquidus phase with melilite as the next crystallizing mineral. However, the bulk CaO content of the White Angel (~40 wt%) is 10% higher and the Al_2O_3 content is about 13% lower than that in type A inclusions (Beckett 1986; MacPherson et al. 1988) and the inclusion is also relatively depleted in Mg (Mg/Si ~0.14 compared to ~1.06 in C1). For this unusual composition, melilite is the phase at the liquidus, explaining the lack of spinel crystals in the core of the White Angel.

Wollastonite is the next phase to crystallize after melilite (~1350 °C) in agreement with the SiO_2 -CaO- Al_2O_3 phase diagram (in Levin et al. 1964) for such a Ca-rich liquid, where the trend of residual liquid produced during equilibration crystallization from a melt with the bulk composition of the White Angel is illustrated. These three elements represent 95% of the bulk inclusion. In the case of the White Angel, there was simply not enough MgO in the melt to form pyroxene (fassaïte) crystals. This phase diagram should be slightly modified if we take into consideration the small

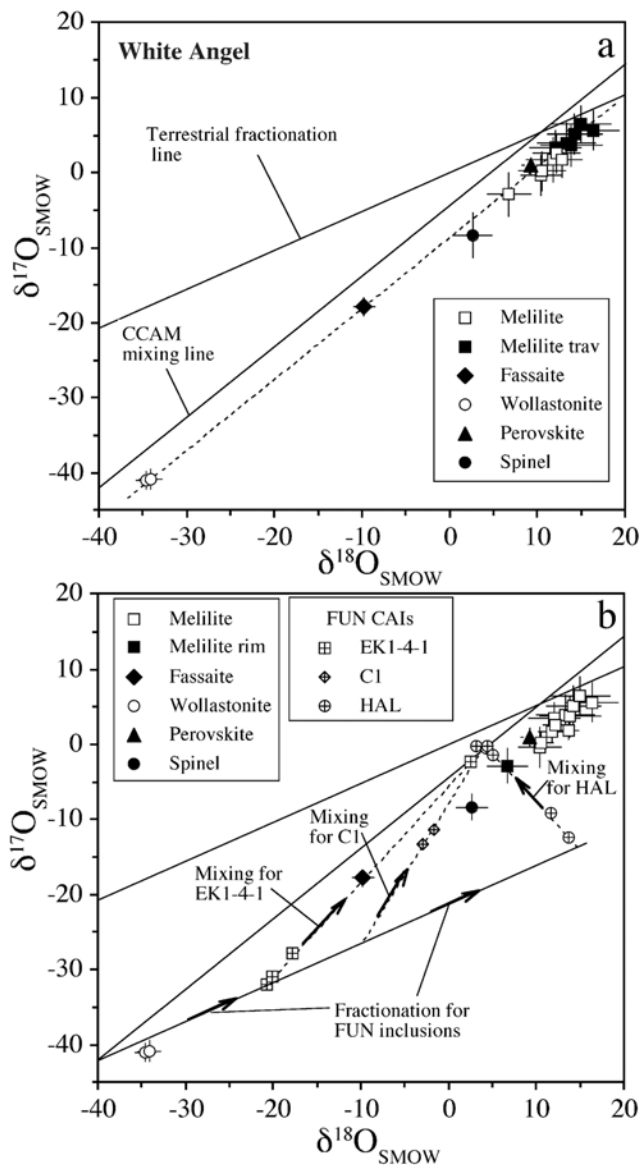


Fig. 17. a) Oxygen isotopic compositions measured in different minerals from the White Angel inclusion are displayed in a three-isotope delta-value plot. Also shown in the plot is the terrestrial fractionation line and the carbonaceous chondrite anhydrous mineral (CCAM) mixing line. b) The O-isotopic ratios in the White Angel are compared to those observed in FUN inclusions. The ratios in the FUN inclusions are explained as fractionation of a ^{16}O -rich composition and subsequent partial isotopic equilibration with a ^{16}O -poor reservoir.

amounts of TiO_2 and MgO accounting for few perovskite and fassaite crystals present, but even in this case we find a large stability field for wollastonite.

Isotopic Mass Fractionation and ^{26}Mg Excess

The inclusion has isotopically heavy Mg, Si, and O (see below) in the interior and Mg smoothly changes to “normal”

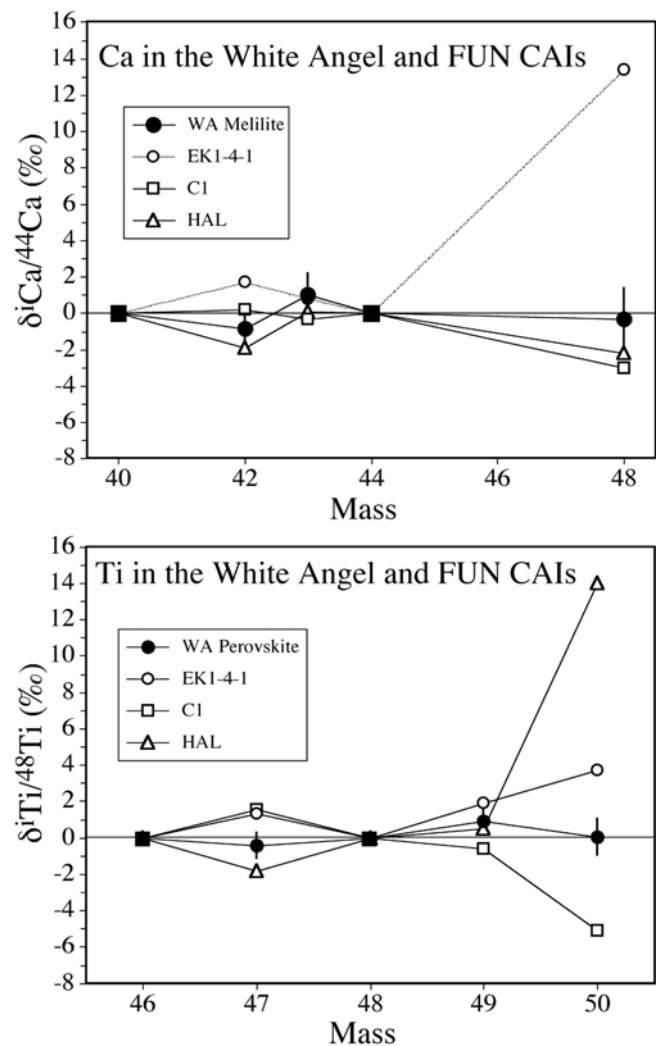


Fig. 18. The Ca and Ti isotopic ratios measured in the White Angel are compared to those observed in FUN inclusions. The fact that Ca and Ti in the White Angel is isotopically normal and that this CAI had a canonical initial $^{26}\text{Al}/^{27}\text{Al}$ ratio indicates that the inclusion is not a FUN inclusion in spite of its large Mg isotopic fractionation.

(unfractionated) at the rim (see Fig. 14). The isotopic fractionation for Mg is larger than for Si, as is commonly observed in most type A and type B CAIs. The fractionation of $\sim 14\text{--}18\text{‰/amu}$ for Mg significantly exceeds the range found in “normal” igneous CAIs ($\sim 10\text{‰/amu}$) (MacPherson et al. 1995) but even larger fractionations have been observed in fluffy type A CAIs (Cosarinsky et al. 2006). It is similar to values reported for FUN inclusions (Clayton et al. 1988). However, we did not find any $\delta^{48}\text{Ca}$ or $\delta^{50}\text{Ti}$ anomalies in melilite or in perovskite (Fig. 18) and therefore the White Angel cannot be designated a FUN inclusion.

Heavy isotope enrichment is usually considered a signature of evaporation. The fact that Mg is isotopically heavy throughout the interior of the inclusion indicates that evaporative loss occurred from a liquid before (or during)

Table 10. Trace element analyses made at Washington University.

Element	Melilite	Wollastonite	Perovskite A	Perovskite B	Perovskite C	Perovskite D	Perovskite E
Li	0.27 ± 0.04	0.010 ± 0.002	0.19 ± 0.06	0.43 ± 0.10	0.049 ± 0.024	0.058 ± 0.020	0.051 ± 0.017
Be	0.53 ± 0.21	0.017 ± 0.002	0.011 ± 0.005	0.52 ± 0.11	0.080 ± 0.025	0.011 ± 0.008	0.034 ± 0.012
B	0.49 ± 0.08	0.34 ± 0.07	1.2 ± 0.3	0.96 ± 0.26	0.81 ± 0.38	0.83 ± 0.29	1.60 ± 0.49
Mg	16,914 ± 47	4696 ± 22	739 ± 21	13,226 ± 123	2209 ± 50	2107 ± 57	5188 ± 78
Al	184,770 ± 379	1790 ± 4	7144 ± 18	65,893 ± 77	11,211 ± 32	3540 ± 21	8858 ± 28.4
Ca	296,535 ± 608	288,499 ± 68	355,000 ± 163	355,000 ± 231	355,000 ± 230	355,000 ± 268	355,000 ± 233
Sc	6.2 ± 0.4	<0.6	67 ± 1	34 ± 2	30.2 ± 1.8	25.8 ± 1.8	32.0 ± 1.9
Ti	1576 ± 9	700 ± 6	330,427 ± 183	291,038 ± 239	360,864 ± 265	364,799 ± 311	351,653 ± 265
V	45.3 ± 0.8	36 ± 1	1571 ± 15	1236 ± 18	1150 ± 18	1496 ± 23	1755 ± 22
Cr	21.7 ± 0.7	8.9 ± 0.6	50 ± 3	41 ± 4	24.1 ± 3.0	32.3 ± 3.2	34.1 ± 3.6
Mn	67.3 ± 1.3	4.0 ± 0.3	3.1 ± 0.7	52 ± 5	7.3 ± 1.5	6.0 ± 0.9	12.2 ± 1.7
Co	12.4 ± 0.9	16 ± 1	30.2 ± 3.7	45 ± 6	25.3 ± 3.6	30.1 ± 5.3	31.3 ± 4.7
Sr	232 ± 2	125 ± 2	386 ± 8.4	349 ± 11	399 ± 12	405 ± 14	412 ± 12
Y	0.50 ± 0.07	3.0 ± 0.3	35 ± 2	35 ± 3	38.5 ± 3.4	41.4 ± 4.1	41.3 ± 3.6
Zr	1.2 ± 0.1	0.16 ± 0.11	47 ± 4	46 ± 6	56.1 ± 6.5	52.8 ± 6.5	66.5 ± 6.7
Nb	0.61 ± 0.04	<0.05	402 ± 11	320 ± 14	221 ± 12	184 ± 12	130 ± 9
Ba	44.9 ± 1.4	4.1 ± 0.3	12.4 ± 1.7	13.6 ± 2.2	27.9 ± 3.7	12.9 ± 2.0	9.1 ± 1.5
La	0.18 ± 0.03	0.24 ± 0.07	24.1 ± 2.8	56 ± 6	24.5 ± 3.3	23.7 ± 3.3	19.0 ± 2.4
Ce	0.74 ± 0.07	0.81 ± 0.18	107 ± 7	282 ± 15	91.9 ± 8.3	104.5 ± 10.4	72.6 ± 6.0
Pr	0.085 ± 0.013	0.10 ± 0.04	10.3 ± 1.4	32 ± 4	9.2 ± 1.5	10.7 ± 1.6	6.3 ± 1.2
Nd	0.37 ± 0.04	0.47 ± 0.10	50 ± 5	120 ± 11	41.1 ± 4.1	50.0 ± 4.8	31.9 ± 2.9
Sm	0.16 ± 0.04	0.51 ± 0.13	26 ± 6	46 ± 7	18.9 ± 4.3	18.6 ± 4.4	15.4 ± 2.5
Eu	1.72 ± 0.19	1.1 ± 0.1	4.1 ± 0.7	3.6 ± 0.7	5.4 ± 0.9	4.2 ± 0.7	5.5 ± 0.7
Gd	0.060 ± 0.024	0.21 ± 0.092	5.4 ± 2.6	6.2 ± 5.5	4.7 ± 2.6	4.7 ± 3.0	4.4 ± 2.3
Tb	0.012 ± 0.006	0.035 ± 0.014	0.94 ± 0.49	1.6 ± 0.9	1.0 ± 0.5	1.0 ± 0.5	0.53 ± 0.32
Dy	0.086 ± 0.016	0.41 ± 0.06	6.6 ± 1.2	8.2 ± 1.9	6.1 ± 1.3	7.6 ± 1.4	5.1 ± 0.9
Ho	0.022 ± 0.006	0.064 ± 0.022	1.0 ± 0.3	1.3 ± 0.5	1.1 ± 0.4	1.0 ± 0.3	0.98 ± 0.34
Er	0.066 ± 0.017	0.22 ± 0.05	3.5 ± 0.8	3.3 ± 0.9	3.5 ± 0.8	3.2 ± 0.8	2.7 ± 0.6
Tm	0.039 ± 0.024	0.26 ± 0.05	2.2 ± 0.5	2.0 ± 0.5	2.2 ± 0.6	3.0 ± 0.9	3.0 ± 0.6
Yb	1.45 ± 0.12	7.2 ± 0.5	50 ± 5	54 ± 7	68.5 ± 7.6	61.1 ± 6.4	74.0 ± 6.6
Lu	0.009 ± 0.005	0.030 ± 0.014	0.46 ± 0.16	<0.36	0.43 ± 0.22	0.38 ± 0.25	0.34 ± 0.20

Table 11. Trace element analyses made at Arizona State University.

Element	Melilite	Wollastonite	Fassaite	Perovskite
Sr	245 ± 2	162 ± 3	78 ± 2	471 ± 6
Y	0.40 ± 0.07	4.9 ± 0.5	1.8 ± 0.2	57 ± 2
Zr	0.59 ± 0.14	2.6 ± 0.5	32.1 ± 1.4	75 ± 4
Nb	0.04 ± 0.03	0.05 ± 0.08	0.59 ± 0.18	513 ± 9
La	0.23 ± 0.03	0.44 ± 0.15	0.079 ± 0.015	37 ± 13
Ce	0.66 ± 0.24	1.3 ± 0.5	0.21 ± 0.05	175 ± 69
Pr	0.080 ± 0.032	0.16 ± 0.11	0.033 ± 0.009	19 ± 8
Nd	0.42 ± 0.20	0.68 ± 0.32	0.16 ± 0.07	76 ± 32
Sm	0.16 ± 0.09	0.49 ± 0.26	0.14 ± 0.07	33 ± 11
Eu	1.67 ± 0.06	1.50 ± 0.14	0.40 ± 0.15	6.3 ± 0.8
Gd	0.053 ± 0.038	0.24 ± 0.03	0.062 ± 0.054	13 ± 5
Tb	0.007 ± 0.005	0.034 ± 0.188	0.015 ± 0.004	1.6 ± 0.7
Dy	0.082 ± 0.026	0.32 ± 0.19	0.087 ± 0.020	8.4 ± 2
Ho	0.013 ± 0.012	0.079 ± 0.060	0.016 ± 0.009	1.1 ± 0.2
Er	0.046 ± 0.040	0.32 ± 0.22	0.092 ± 0.020	4.7 ± 0.9
Tm	0.019 ± 0.028	0.29 ± 0.06	0.092 ± 0.019	2.4 ± 0.6
Yb	0.89 ± 0.58	8.8 ± 1.7	3.65 ± 1.04	55 ± 18
Lu	0.006 ± 0.005	0.031 ± 0.024	0.036 ± 0.009	0.04 ± 0.07

crystallization of the constituent phases of the CAI. A fractionation of 18‰/amu implies that ~75% of the Mg was lost by evaporation (Davis et al. 1990), which contributed to the low Mg content of the inclusion. Subsequently, the inclusion must have reacted or equilibrated with “normal” Mg from the surrounding gas (Fahey et al. 1987b; Lin and Kimura 2000; Simon et al. 2005) as is evidenced by the diffusion-like profile (Fig. 14). The fact that no such diffusion profile is seen for Si either reflects more sluggish isotopic self-diffusion or a lack of an exchangeable reservoir above the closure temperature.

Melilite shows clear evidence for nonlinear ^{26}Mg excesses with an inferred $^{26}\text{Al}/^{27}\text{Al}$ ratio of $\sim 5.5 \times 10^{-5}$, which is within error of either the so-called “canonical” initial $^{26}\text{Al}/^{27}\text{Al}$ ratio (MacPherson et al. 1995) or new estimates for a higher solar system initial ratio (Bizzaro et al. 2004, 2005). This is another feature which distinguishes the White Angel from FUN inclusions which typically lack evidence for ^{26}Al decay. Equilibration with isotopically unfractionated Mg in the regions close to the rim (Fig. 14) had to occur shortly after formation, within a few hundred thousand years, to preserve the roughly canonical ratio.

Source Conditions: Constrains from the Rare Earth Elements

The fractionation of REEs offers one of the best ways of distinguishing the primary cosmo-chemical processes from the later, secondary processes. All phases in this inclusion show the imprint of the overall pattern of the whole inclusion (Figs. 19 and 20). This pattern, with excesses in the most volatile elements Eu and Yb, is an inverted ultrarefractory pattern (see, e.g., Ireland and Fegley 2000). It indicates condensation from a reservoir depleted in the most refractory REE (the heavy REEs [HREEs]) as well as Y and Zr. This reservoir was also depleted in Al as the

low Al/Ca ratio of the inclusion shows. The REE pattern of the White Angel has some similarities with the group II pattern (Martin and Mason 1974). Boynton (1975) showed that the group II pattern, which shows depletion in the most refractory and most volatile REEs, requires removal of the most refractory elements and subsequent condensation of all but the most volatile elements. Thus Eu and Yb are low in classical group II patterns. In contrast, Eu and Yb are the most abundant elements of the REE pattern of the whole White Angel inclusion. This means that after removal of an ultrarefractory component (Sc [$1.1 \times \text{CI}$], V [$1.4 \times \text{CI}$], Y [$1.1 \times \text{CI}$], and Zr [$0.61 \times \text{CI}$] are $\sim 1 \times \text{CI}$, as are the HREEs), all remaining REE elements, but also other relatively volatile elements such as Nb, Ca, and Sr, fully condensed into the precursor mineral(s) of the inclusion (the abundance/CI chondrite = 28 for Sr and Nb and 31.5 for Ca). The removal of the ultrarefractory component probably was the result of the condensation of highly refractory minerals, such as hibonite or corundum, from a solar gas. Condensation calculations showed that hibonite is a likely candidate (MacPherson and Davis 1994). The UR elements cannot have condensed into perovskite (Davis and Grossman 1979) because the Eu abundance is about the same as that of Ca ($30 \times \text{CI}$) and the Yb abundance is the same as that of Ti. They likely were fractionated from Ti during separation from the less refractory trace elements and in this process perovskite was not an actor. Spinel cannot have been responsible for the Al depletion because the refractory trace elements do not tend to go into spinel. The condensation of the White Angel precursors probably occurred soon after removal and isolation of the ultrarefractory component from the gas. The high abundance of Eu and Yb is evidence that the condensation temperature was lower than the temperature at which type II inclusions condensed.

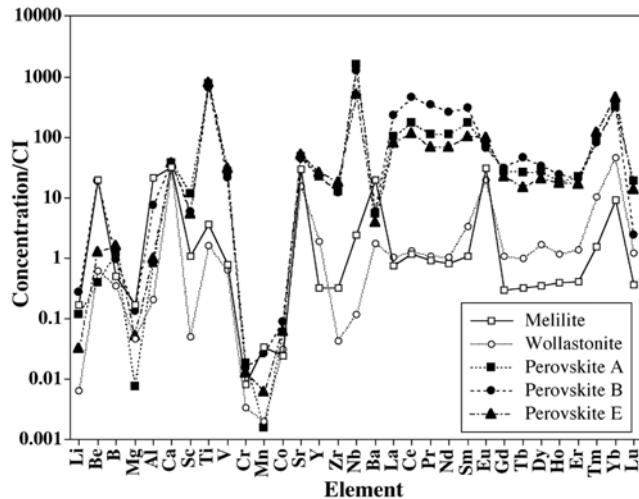


Fig. 19. CI-normalized abundance patterns of trace elements in different minerals from the White Angel refractory inclusion. Volatile elements such as Cr and Mn are strongly depleted ($\text{Cr} = 0.01 \times \text{CI}$, $\text{Mn} = 0.03 \times \text{CI}$). However, trace elements such as Sr, Nb, Eu, and Yb, which are less refractory than highly refractory elements such as Y, Zr, and the HREEs, are strongly enhanced. (Abundance element/CI chondrite: Al = 14.5, Ca = 31.5, Ti = 22, Si = 1.3, Mg = 0.2, Sc = 1.1, V = 1.4, Sr = 28, Y = 1.1, Zr = 0.61, Nb = 28).

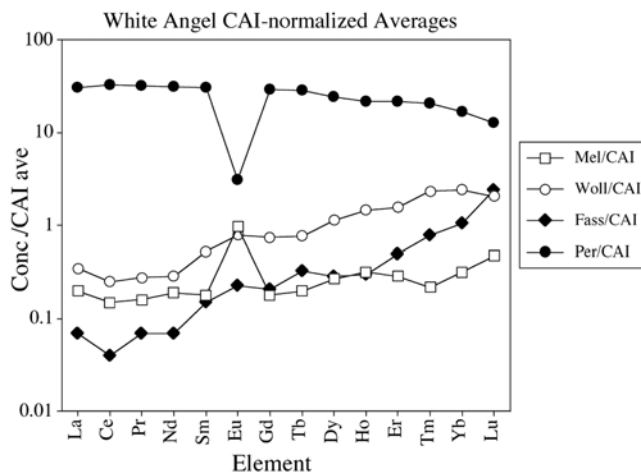


Fig. 21. REE patterns of minerals in the White Angel CAI normalized to the abundance pattern of the whole inclusion. These mineral patterns reflect igneous partitioning between minerals during crystallization from a melt.

The patterns of the individual minerals (Figs. 19 and 20) derive from the whole CAI pattern by igneous partitioning between the crystal and the melt, regardless of the location within the CAI (Fig. 21). Partitioning between perovskite and melilite has been seen in many CAIs (e.g., Fahey et al. 1987b; El Goresy et al. 2002). The depletion of Eu in perovskite and the excess of Eu in melilite relative to the bulk CAI indicate crystallization from a melt. This positive Eu anomaly in melilite crystals usually indicates the presence of Eu^{2+} , which is preferentially stripped out by melilite. Therefore, the patterns

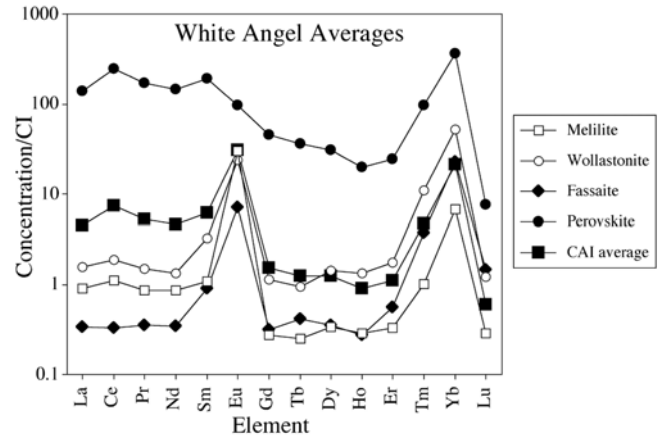


Fig. 20. CI-normalized REE abundance patterns of the averages of various White Angel minerals. Also shown is the abundance pattern of the whole inclusion as determined from those of the individual minerals and their modal abundances. The overall pattern is the inversion of an ultrarefractory REE pattern, indicating that the White Angel formed from material from which the ultrarefractory elements had been removed.

of the individual phases in the White Angel are consistent with the interpretation that the core was once molten.

An interesting case is the abundance of Ce in the whole inclusion. As already mentioned, the Mg isotopic fractionation implies a Mg loss of ~75%. For this amount of Rayleigh distillation, and given an initial chondritic composition, a substantial Ce depletion is expected (Floss et al. 1996). However, the liquid droplet from which Mg was lost by evaporation had a composition that was far from chondritic and, because Mg was low to start with, the loss of 75% MgO constitutes a loss of only 2.8% of the whole CAI (see Table 5). Thus, it is not clear what the effect on the Ce would have been. If Ce was indeed lost during the Rayleigh distillation, it could have been that there was an excess of Ce in the original precursor material. Some hibonites have an ultrarefractory pattern and large Ce depletion (e.g., hibonite 7-404 in Ireland et al. 1988) and the complementary material must have had a large Ce excess. There is even a small Ce excess in the REE pattern of the White Angel (Fig. 20). But MacPherson et al. (1988) pointed out that trace element fractionation patterns are decoupled and often conflicting with isotopic signatures and even sometimes with bulk element chemistry. This is compatible with our model because REE are more refractory than Mg and Si.

The Puzzling Oxygen Isotopic Composition

On the oxygen three-isotope plot, all minerals have isotopically fractionated oxygen with the same fractionation but with different degrees of ^{16}O excesses. Oxygen isotopic compositions of anhydrous minerals of the White Angel fall along a line of slope 1 parallel to the CCAM line (Fig. 17a).

Wollastonite has the largest ^{16}O excess; perovskite and melilite have no ^{16}O excess but have a strikingly similar degree of isotopic fractionation as the other phases in the inclusion. This isotopic composition is difficult to understand if the White Angel formed, like most refractory inclusions, in an initially ^{16}O -rich environment, and later interacted and partially equilibrated with a ^{16}O -poorer nebular gas (Clayton 2002; Krot et al. 2005). That the O-isotopic composition of the White Angel is fractionated is expected in view of the large isotopic fractionation of Mg and Si. However, the White Angel did not follow the same two-stage process invoked for FUN inclusions, namely: 1) mass-dependent fractionation of an originally ^{16}O -rich composition, moving that composition along a slope one-half line in the O three-isotope plot (see Fig. 17b); and 2) exchange with a common external reservoir to produce for each FUN inclusion a line converging to a common composition lying on the CCAM mixing line (Fig. 17b). In contrast, even the ^{16}O -poor phases in the White Angel are fractionated relative to the CCAM mixing line.

Just as with FUN inclusions and the F inclusions TE and CG-14, the precursors of the White Angel were rich in ^{16}O and evaporation from a liquid droplet fractionated this original composition. However, in this case, the various minerals must have experienced later equilibration within an ^{16}O -poor reservoir that was itself fractionated relative to (i.e., shifted to the right of) the CCAM mixing line. This fractionated ^{16}O -poor reservoir could be the result of fluid-rock interaction and indeed, the O-isotopic compositions of several CM chondrites (Clayton and Mayeda 1999) lie close to ^{16}O -poor end of the White Angel mixing line. Recent ion microprobe analyses (Cosarinsky et al. 2003) also showed that the O-isotopic ratios of iron-rich silicates, in particular together with “secondary” wollastonite, in and around an Allende CAI, define a slope-1/2 line near the upper end of the CCAM line and below the terrestrial fractionation line. The most ^{18}O -rich points of this array lie on a correlation line with our White Angel data. These authors suggested low-temperature parent body processes as a cause for their array and Krot et al. (1998) attributed the scattering toward more ^{18}O -rich compositions to hydrous alteration in a parent body. A mass-fractionation trend near the upper end of the CCAM line has also been identified based on the analysis of Allende chondrules and a CAI (Young et al. 1999). This “Allende mass fractionation” (AMF) line is considered to result from relatively low-temperature isotopic exchange between rock and a flowing fluid during reactive transport on the meteorite parent body (Young et al. 1999). The most ^{16}O -poor melilite grains in the White Angel are compatible with the AMF. Although the parent body of Leoville is not believed to have undergone extensive hydrous alteration processes, such as would result in massive mineralogical changes, it is possible that there exists a low-temperature overprint on oxygen isotopic compositions due to partial equilibration with an aqueous fluid. We cannot resolve any distribution of O-isotopic ratios in the White Angel along

slope-1/2 lines but our data may not be sufficiently precise to reveal such trends.

The degree of preservation of ^{16}O -enrichment among the various mineral phases of the White Angel shows some similarities with mineralogic control of O-isotopic compositions in CV CAIs, but some surprises as well. As expected, melilite shows the largest amount of isotopic equilibration with an ^{16}O -poor (fluid?) reservoir. In most CV CAIs, Mg-Al spinel is usually found to be the most ^{16}O -rich phase, along with pyroxene and hibonite (if present). The White Angel spinel grains are very small and O-isotopic analyses likely suffered contamination by beam overlap onto melilite, the relatively ^{16}O -poor measured composition probably doesn't reflect the true compositions of the spinels. In contrast, perovskite grains are large and the ion probe data clearly indicate that this phase is relatively ^{16}O -poor. Although it might appear surprising that perovskite has equilibrated O isotopes with a ^{16}O -poor reservoir to the same extent as melilite, the relevant diffusion data are lacking. Although the ^{16}O -rich composition of wollastonite is generally compatible with slow diffusion of oxygen in Ca-rich pyroxene, the intermediate composition of the fassaite is also somewhat unexpected (Ryerson and McKeegan 1994). Overall, the distribution of oxygen isotopes within the White Angel reflects a complex history involving mass fractionation at high temperatures (above the solidus) and partial equilibration of different mineral phases with a heavy-oxygen reservoir, possibly at low temperatures in a parent-body setting. The secondary exchange could also have been at higher temperatures, but in this case the gaseous reservoir had an unusually heavy isotopic composition that was mass-fractionated from the CCAM line.

CONCLUSIONS

We have described a unique compact type A refractory inclusion in the Leoville CV3 chondrite that contains large equant wollastonite crystals. On the basis of the petrologic, isotopic, and trace-element characteristics, we conclude that White Angel represents an original refractory assemblage in which wollastonite is a primary phase. A scenario explaining the presence of wollastonite in White Angel as secondary mineral is rejected. Indeed, this inclusion cannot represent an agglomerate of various components (such as fluffy type A inclusions with secondary wollastonite needles) that was later melted for the following reasons: 1) the presence of a large positive ^{16}O anomaly in wollastonite crystals; 2) the occurrence of a canonical $^{26}\text{Al}/^{27}\text{Al}$ ratio in melilite crystals; 3) the absence of relict grains; 4) the bulk composition of White Angel, which is not enriched in SiO_2 but rather depleted in Al_2O_3 ; and 5) the scarcity of FeO and Na_2O , oxides that could have been incorporated into secondary crystals. Thus, melting did not follow secondary mineralization of the precursor material by sodium-bearing fluid or gas.

We propose the following scenario for the formation history of the White Angel:

1. Removal of ultrarefractory elements (Al, HREEs) from a gas of solar composition by condensation of refractory mineral phases, possibly including hibonite.
2. Condensation of precursor phases from this reservoir, which contains ^{26}Al at the canonical abundance, at a relatively low temperature so that the most volatile REEs Eu and Yb, as well as Ca, Sr, and Nb fully condensed.
3. Melting of precursors and prolonged heating of the liquid, which caused evaporation of Mg and some Si from this molten droplet and led to isotopic fractionation of Mg, Si, and O.
4. Our results suggest that this droplet started to crystallize melilite, the major mineral phase. Wollastonite crystallized as a primary phase because of the high Ca and low Al content of the melt. The existence of symplectites and the presence of trapped idiomorphic melilite crystals indicate rapid growth from this melt. Moreover, the high Ti^{3+} contents of the pyroxene crystals indicates that reducing conditions must have prevailed during crystallization of the White Angel.
5. At a later time, but before significant decay of ^{26}Al occurred, partial exchange with a gaseous reservoir containing unfractionated Mg took place, resulting in a diffusion profile of the Mg isotopic fractionation close to the border of the CAI.
6. Partial isotopic equilibration of oxygen in different minerals with possibly the same gaseous reservoir occurred. This reservoir must have had a fairly unusual O-isotopic composition close to $\delta^{17}\text{O} \sim 10\text{‰}$ and $\delta^{18}\text{O} \sim 20\text{‰}$, which is thus quite different from the equilibrium isotopic composition of O in FUN and other F inclusions but similar to the isotopic composition exhibited by some CM and CI chondrites. It is also possible that isotopic exchange occurred at lower temperatures with a parent body fluid.
7. Deformation of the inclusion during or after incorporation into the Leoville parent body. The complex multistage record history of the White Angel inclusion happened in a relatively brief period of time, before substantial decay of ^{26}Al .

Acknowledgments—The study of this CAI was conducted while C. C. was a post-doctorate fellow at Arizona State University, USA. Many thanks are due to Carleton B. Moore (ASU) for the loan of the Leoville thin section. We are grateful to Jim Clark and Joachim Janicke for their kind assistance at the electron microprobes. Discussions with Alexander Krot and fruitful suggestions from Ahmed El Goresy are appreciated. We are grateful for constructive comments on behalf of associate editor Ed Scott, and two reviewers, Steve Simon and Alexander Krot. The first author

especially wants to thank co-author Ernst Zinner who motivated her to surface after a long episode taken to care for her three beloved children. The UCLA ion microprobe laboratory is partially supported by grant from NSF Instrumentation and Facilities program. This work was also supported by NASA Grants NNG04GG49G (E. Z.) and NNG06GF08G (P. B.).

Editorial Handling—Dr. Edward Scott

REFERENCES

- Albee A. L. and Ray L. 1971. Correction factors for electron probe microanalysis of silicates, oxides, carbonates, phosphates, and sulfates. *Analytical Chemistry* 42:1408–1414.
- Allen J. M., Grossman L., Davis A. M., and Hutcheon I. D. 1978. Mineralogy, textures, and mode of formation of a hibonite-bearing Allende inclusion. Proceedings, 9th Lunar and Planetary Science Conference. pp. 1209–1233.
- Allen J. M. and Grossman L. 1978. Solar nebula condensation: Implications from Allende inclusion mineralogy. *Meteoritics* 13: 383–384.
- Amelin Y., Krot A. N., Hutcheon I. D., and Ulyanov A. A. 2002. Lead isotopic ages of chondrules and calcium-aluminum-rich inclusions. *Science* 297:1678–1683.
- Anders E. and Grevesse N. 1989. Abundances of the elements: Meteoritic and solar. *Geochimica et Cosmochimica Acta* 53:197–214.
- Barber D. J., Martin P. M., and Hutcheon I. D. 1984. The microstructures of minerals in coarse-grained Ca-Al-rich inclusions from the Allende meteorite. *Geochimica et Cosmochimica Acta* 48:769–783.
- Beckett J. R. 1986. The origin of calcium-, aluminum-rich inclusions from carbonaceous chondrites: An experimental study. Ph.D. thesis, The University of Chicago, Chicago, Illinois, USA.
- Beckett J. R. and Grossman L. 1986. Oxygen fugacities in the solar nebula during crystallization of fassaite in Allende inclusions. Proceedings, 17th Lunar and Planetary Science Conference. pp. 36–37.
- Beckett J. R. and Stolper E. 1994. The stability of hibonite, melilite and other aluminous phases in silicate melts: Implications for the origin of hibonite-bearing inclusions from carbonaceous chondrites. *Meteoritics* 29:41–65.
- Beckett J. R. and Stolper E. 2000. The partitioning of Na between melilite and liquid: Part I. The role of crystal chemistry and liquid composition. *Geochimica et Cosmochimica Acta* 64: 2509–2517.
- Beckett J. R., Connolly H. C., and Ebel D. S. 2006. Chemical processes in igneous calcium-aluminum-rich inclusions: A mostly CMAS view of melting and crystallization. In *Meteorites and the early solar system*, vol. 2, edited by Lauretta D. S. and McSween H. Y., Jr. Tucson, Arizona: The University of Arizona Press. pp. 399–429.
- Bence A. E. and Albee A. L. 1968. Empirical correction factors for the electron microanalysis of silicates and oxides. *The Journal of Geology* 76:382–403.
- Bizzarro M., Baker J. A., and Haack H. 2004. Mg isotope evidence for contemporaneous formation of chondrules and refractory inclusions. *Nature* 431:275–278.
- Bizzarro M., Baker J. A., and Haack H. 2005. Mg isotope evidence for contemporaneous formation of chondrules and refractory inclusions (corrigendum). *Nature* 435:1280.
- Boynton W. V. 1975. Fractionation in the early solar nebula:

- Condensation of yttrium and the rare earth elements. *Geochimica et Cosmochimica Acta* 39:569–584.
- Brearley A. J. and Jones R. H. 1998. Chondritic meteorites. In *Planetary materials*, edited by Papike J. J. Washington, D.C.: Mineralogical Society of America. 36:3-01–3-398.
- Caillet C. and Buseck P. R. 1992. The “White Angel”: A wollastonite-bearing refractory inclusion in the Leoville chondrite (abstract). *Meteoritics* 27:208.
- Caillet C., MacPherson G. J., and Zinner E. K. 1993. Petrologic and Al-Mg isotopic clues to the accretion of two refractory inclusions onto the Leoville parent body: One was hot, the other wasn't. *Geochimica et Cosmochimica Acta* 57:4725–4743.
- Catanzaro E. J., Murphy T. J., Garner E. L., and Shields W. R. 1966. Absolute isotopic abundance ratios and atomic weights of magnesium. *Journal of Research of the National Bureau of Standards and Technology* 70a:453–458.
- Christophe Michel-Levy M. 1968. Un chondre exceptionnel dans la meteorite de Vigarano. *Bulletin de la Société Française de Minéralogie et de Cristallographie* 91:212–214.
- Clayton R. N. 2002. Self shielding in the solar nebula (abstract). *Nature* 415:860–861.
- Clayton R. N. and Mayeda T. K. 1999. Oxygen isotope studies of carbonaceous chondrites. *Geochimica et Cosmochimica Acta* 63: 2089–2104.
- Clayton R. N., Hinton R. W., and Davis A. M. 1988. Isotopic variations in the rock-forming elements in meteorites. *Philosophical Transactions of the Royal Society A* 325:483–501.
- Clayton R. N., MacPherson G. J., Hutcheon I. D., Davis A. M., Grossman L., Mayeda T. K., Molini-Velsko C., Allen J. M., and El Goresy A. 1984. Two forsterite-bearing FUN inclusions in the Allende meteorite. *Geochimica et Cosmochimica Acta* 48:535–548.
- Clayton R. N., Onuma N., Grossman L., and Mayeda T. K. 1977. Distribution of the pre-solar component in Allende and other carbonaceous chondrites. *Earth and Planetary Science Letters* 34: 209–224.
- Cosarinsky M., Leshin L. A., MacPherson G. J., Krot A. N., and Guan Y. 2003. Oxygen isotopic composition of Ca-Fe-rich silicates in and around an Allende Ca-Al-rich inclusion (abstract #1043). 34th Lunar and Planetary Science Conference. CD-ROM.
- Cosarinsky M., Taylor D. J., and McKeegan K. D. 2006. Aluminum-26 model ages of hibonite and spinel from type A inclusions in CV chondrites (abstract #2357). 37th Lunar and Planetary Science Conference. CD-ROM.
- Davis A. and Grossman L. 1979. Condensation and fractionation of rare earth elements in the solar nebula. *Geochimica et Cosmochimica Acta* 43:1611–1632.
- Davis A. M., Hashimoto A., Clayton R. N., and Mayeda T. K. 1990. Isotope mass fractionation during evaporation of Mg_2SiO_4 . *Nature* 347:655–658.
- Dowty E. and Clark J. R. 1973. Crystal structure refinement and optical properties of a Ti^{3+} fassaite from the Allende meteorite. *American Mineralogist* 58:230–242.
- Ebel D. S. and Grossman L. 2000. Condensation in dust-enriched systems. *Geochimica et Cosmochimica Acta* 64:339–366.
- El Goresy A., Nagel K., and Ramdohr P. 1977. Type A Ca-Al-rich inclusions in Allende meteorite: Origin of the perovskite-fassaite symplectite around rhonite and chemistry and assemblages of the refractory metals (mo, W) and platinum metals (Ru, Os, Ir, Re, Rh, Pt). *Meteoritics* 12:216.
- El Goresy A., Palme H., Yabuki H., Nagel K., Herrwerth I., and Ramdohr P. 1984. A calcium-aluminum-rich inclusion from the Essebi (CM2) chondrite: Evidence for captured spinel-hibonite spherules and for an ultra-refractory rimming sequence. *Geochimica et Cosmochimica Acta* 48:2283–2298.
- El Goresy A., Zinner E., Caillet C., Virag A., and Weinbruch S. 1991. Allende TE: Evidence for multiple isotopic fractionation events before and after oxidation and alteration. *Proceedings, 22nd Lunar and Planetary Science Conference*. pp. 345–346.
- El Goresy A., Zinner E., Matsunami S., Palme H., Spettel B., Lin Y., and Nazarov M. 2002. Efremovka 101.1: A CAI with ultrarefractory REE patterns and enormous enrichments of Sc, Zr, and Y in fassaite and perovskite. *Geochimica et Cosmochimica Acta* 66:1459–1491.
- Fahey A. J., Goswami J. N., McKeegan K. D., and Zinner E. 1987a. ^{26}Al , ^{244}Pu , ^{50}Ti , REE, and trace element abundances in hibonite grains from CM and CV meteorites. *Geochimica et Cosmochimica Acta* 51:329–350.
- Fahey A. J., Zinner E. K., Crozaz G., and Kornacki A. S. 1987b. Microdistributions of Mg isotopes and REE abundances in a type A calcium-aluminum-rich inclusion from Efremovka. *Geochimica et Cosmochimica Acta* 51:3215–3229.
- Fegley B., Jr. and Ireland T. R. 1991. Chemistry of the rare earth elements in the solar nebula. *European Journal of Solid State and Inorganic Chemistry* 28:335–346.
- Floss C., El Goresy A., Zinner E., Kransel G., Rammansee W., and Palme H. 1996. Elemental and isotopic fractionations produced through evaporation of the Allende CV chondrite: Implications for the origin of HAL-type hibonite inclusions. *Geochimica et Cosmochimica Acta* 60:1975–1997.
- Grossman L. 1972. Condensation in the primitive solar nebula. *Geochimica et Cosmochimica Acta* 36:597–619.
- Grossman L. 1975. Petrography and mineral chemistry of Ca-rich inclusions in the Allende meteorite. *Geochimica et Cosmochimica Acta* 39:433–454.
- Ireland T. R. 1990. Presolar isotopic and chemical signatures in hibonite-bearing refractory inclusions from the Murchison carbonaceous chondrite. *Geochimica et Cosmochimica Acta* 54: 3219–3237.
- Ireland T. R. and Fegley B., Jr. 2000. The solar system's earliest chemistry: Systematics of refractory inclusions. *International Geology Review* 42:865–894.
- Ireland T. R., Fahey A. J., and Zinner E. K. 1988. Trace-element abundances in hibonites from the Murchison carbonaceous chondrite: Constraints on high-temperature processes in the solar nebula. *Geochimica et Cosmochimica Acta* 52:2841–2854.
- Ireland T. R., Fahey A. J., and Zinner E. K. 1991. Hibonite-bearing microspherules: A new type of refractory inclusions with large isotopic anomalies. *Geochimica et Cosmochimica Acta* 55: 367–379.
- Kimura M., El Goresy A., Palme H., and Zinner E. 1993. Ca-, Al-rich inclusions in the unique chondrite ALH 85085: Petrology, chemistry, and isotopic compositions. *Geochimica et Cosmochimica Acta* 57:2329–2359.
- Krot A. N., Petaev M. I., Scott E. R. D., Choi B.-G., Zolensky M. E., and Keil K. 1998. Progressive alteration in CV3 chondrites: More evidence for asteroidal alteration. *Meteoritics & Planetary Science* 33:1065–1085.
- Krot A. N., Hutcheon I. D., Yurimoto H., Cuzzi J. N., McKeegan K. D., Scott E. R. D., Libourel G., Chaussidon M., Aleon J., and Petaev M. I. 2005. Evolution of oxygen isotopic composition in the inner solar nebula. *The Astrophysical Journal* 622:1333–1342.
- Lee T. 1988. Implications of iostopic anomalies for nucleosynthesis. In *Meteorites and the early solar system*, edited by Kerridge J. F. and Matthews M. S. Tucson, Arizona: The University of Arizona Press. pp. 1063–1089.
- Levin E. M., Robbins C. R., and MacMurdie H. F. 1964. *Phase diagrams for ceramists*. Westerville, Ohio: The American Ceramic Society. 601 p.

- Lin Y. and Kimura M. 2000. Two unusual type B refractory inclusions in the Ningqiang carbonaceous chondrite—Evidence for relicts, xenoliths and multi-heating. *Geochimica et Cosmochimica Acta* 64:4031–4047.
- MacPherson G. J. 2003. Calcium-aluminum-rich inclusions in chondritic meteorites. In *Meteorites, comets, and planets*, edited by Davis A. M. Treatise on Geochemistry, vol. 1. Oxford: Elsevier-Pergamon. pp. 201–246.
- MacPherson G. J., Davis A. M., and Zinner E. K. 1995. The distribution of aluminum-26 in the early solar system—A reappraisal. *Meteoritics* 30:365–386.
- MacPherson G. J. and Huss G. R. 2005. Petrogenesis of Al-rich chondrules: Evidence from bulk compositions and phase equilibria. *Geochimica et Cosmochimica Acta* 69:3099–3127.
- MacPherson G. J., Paque J. M., Stolper E., and Grossman L. 1984. The origin and significance of reverse zoning in melilite from Allende type B inclusions. *Journal of Geology* 92:289–305.
- MacPherson G. J., Wark D. A., and Armstrong J. T. 1988. Primitive material surviving in chondrites: Refractory inclusions. In *Meteorites and the early solar system*, edited by Kerridge J. F. and Matthews M. S. Tucson, Arizona: The University of Arizona Press. pp. 746–807.
- MacPherson G. J. and Davis A. M. 1994. Refractory inclusions in prototypical CM chondrite, Mighei. *Geochimica et Cosmochimica Acta* 58:5599–5625.
- Martin P. M. and Mason B. 1974. Major and trace elements in Allende meteorite. *Nature* 249:333–334.
- McKeegan K. D. 1987. Oxygen isotopes in refractory stratospheric dust particles: Proof of extraterrestrial origin. *Science* 237:1468–1471.
- McKeegan K. D., Leshin L. A., Russell S. S., and MacPherson G. J. 1998. Oxygen isotopic abundances in calcium-aluminum-rich inclusions from ordinary chondrites: Implications for nebular heterogeneity. *Science* 280:414–418.
- McKeegan K. D., Walker R. M., and Zinner E. 1985. Ion microprobe isotopic measurements of individual interplanetary dust particles. *Geochimica et Cosmochimica Acta* 49:1971–1987.
- Niederer F. R. and Papanastassiou D. A. 1984. Ca isotopes in refractory inclusions. *Geochimica et Cosmochimica Acta* 48:1279–1293.
- Niederer F. R., Papanastassiou D. A., and Wasserburg G. J. 1985. Absolute isotopic abundances of Ti in meteorites. *Geochimica et Cosmochimica Acta* 49:835–851.
- Paque J. M., Beckett J. R., Barber D. J., and Stolper E. M. 1994. A new titanium-bearing calcium aluminosilicate phase: I. Meteoritic occurrences and formation in synthetic systems. *Meteoritics* 29:673–682.
- Ryerson F. J. and McKeegan K. D. 1994. Determination of oxygen self-diffusion in akermanite, anorthite, diopside, and spinel: Implications for oxygen isotopic anomalies and the thermal histories of Ca-Al-rich inclusions. *Geochimica et Cosmochimica Acta* 58:3713–3734.
- Simon J. I., Young E. D., Russell S. S., Tonui E. K., Dyl K. A., and Manning C. E. 2005. A short time scale for changing oxygen fugacity in the solar nebula revealed by high-resolution ^{26}Al - ^{26}Mg dating of CAI rims. *Earth and Planetary Science Letters* 238:272–283.
- Simon S. B., Davis A. M., and Grossman L. 1999. Origin of compact type A refractory inclusions from CV3 carbonaceous chondrites. *Geochimica et Cosmochimica Acta* 63:1233–1248.
- Simon S. B., McKeegan K. D., Ebel D. S., and Grossman L. 2000. Complexly zoned chromium-aluminum spinel found in situ in the Allende meteorite. *Meteoritics & Planetary Science* 35:215–227.
- Simon S. B. and Grossman L. 2004. A preferred method for the determination of bulk compositions of coarse-grained refractory inclusions and some implications of the results. *Geochimica et Cosmochimica Acta* 68:4237–4248.
- Simon S. B. and Grossman L. 2006. A comparative study of melilite and fassaite in type B1 and B2 refractory inclusions. *Geochimica et Cosmochimica Acta* 70:780–798.
- Stolper E. 1982. Crystallization sequences of Ca-Al-rich inclusions from Allende: An experimental study. *Geochimica et Cosmochimica Acta* 46:2159–2180.
- Wark D. and Boynton W. B. 2001. The formation of rims on calcium-aluminum-rich inclusions: Step I—Flash heating. *Meteoritics & Planetary Science* 36:1135–1166.
- Wark D. and Lovering J. F. 1977. Marker events in the early solar system: Evidence from rims on Ca-Al-rich inclusions in carbonaceous chondrites. Proceedings, 8th Lunar Science Conference. pp. 95–112.
- Wass S. Y. 1973. The origin and petrogenetic significance of hour-glass zoning in titaniferous clinopyroxenes. *Mineralogical Magazine* 39:1–144.
- Weber D., Zinner E., and Bischoff A. 1995. Trace element abundances and Mg, Ca, and Ti isotopic compositions of grossite-containing inclusions from the carbonaceous chondrite Acfer 182. *Geochimica et Cosmochimica Acta* 59:803–823.
- Young E. D., Ash R. D., England P., and Rumble D. 1999. Fluid flow in chondritic parent bodies: Deciphering the compositions of planetesimals. *Science* 286:1331–1335.
- Young E. D., Simon J. I., Galy A., Russell S. S., Tonui E., and Lovera O. 2005. Supra-canonical $^{26}\text{Al}/^{27}\text{Al}$ and the residence time of CAIs in the solar protoplanetary disk. *Science* 308:223–227.
- Zinner E. and Crozaz G. 1985. A method for the quantitative measurement of rare earth elements in the ion microprobe. *International Journal of Mass Spectrometry and Ion Processes* 69:17–38.
- Zinner E. and Crozaz G. 1986. Ion probe determination of the abundances of all the rare earth elements in single mineral grains. In *Secondary ion mass spectrometry (SIMS V)*, edited by Benninghoven A., Colton R. J., Simons D. S., and Werner H. W. Berlin, Heidelberg, New York: Springer-Verlag. pp. 444–446.
- Zinner E. K., Fahey A. J., Goswami J. N., Ireland T. R., and McKeegan K. D. 1986. Large ^{48}Ca anomalies are associated with ^{50}Ti anomalies in Murchison and Murray hibonites. *The Astrophysical Journal* 311:L103–L107.